UNIVERSITÀ DEGLI STUDI DI PADOVA

UNIVERSITA' DEGLI STUDI DI PADOVA

Dipartimento di Ingegneria Industriale DII

Corso di Laurea Magistrale in Ingegneria dell'Energia Elettrica

Analytical Design Concept for Synchronous Reluctance Machines

Relatore: Prof. Nicola Bianchi

Correlatore: Prof. Hans Georg Herzog

Matteo Boggian 1134528

Anno Accademico 2017/2018

Abstract

In order to reduce greenhouse gases emissions and environment pollution, the research and development of low environmental impact technological solutions embrace every industrial sectors. Transport sector electrification gained wide interest in order to limit the CO_2 emissions. Pure electric vehicles and hybrid electric vehicles are about to enter the mass market thanks to the rapid advances in technology and expected drop in the new models prices. In order to fully embrace electric mobility as soon as possible, the problems related to this technology must be faced up and solved by automotive manufacturers and energy providers.

Automotive manufacturers focus on different vehicle powertrain solutions in efficiency and cost saving terms. Electric motor is the core of the vehicle powertrain and it defines the overall vehicle performances. Synchronous reluctance motors have been re-considered in order to evaluate their competitiveness for electric traction applications. The unique rotor topology of synchronous reluctance motors guarantees electrical and mechanical features that make it perfectly suited for intermittent operating conditions and for severe demanding applications like the typical urban road vehicle traction characteristic.

The aim of the thesis is to derive an analytical design concept based on mathematical and physical model of synchronous reluctance machines working principles. The design concept general validity allows to adopt it for any application specifications and requirements. Magnetic, electrical and mechanical aspects are investigated to maximize the motor performances in high torque density and efficiency terms.

In chapter [2] the electromagnetic torque generation of rotating electric machines is investigated and described through a simplified model. In particular a synchronous reluctance machine simplified model is analytically obtained and adopted as design basis.

In chapter [3] the analytical design concept is presented. Starting from the magnetic loading assumption, the electrical loading and the machine size are obtained. Successively the stator and rotor geometry are designed. The rotor topology design is considered with particular attention from an electromagnetic and both mechanical point of view. The parameters influencing the motor performances are individually investigated in order to identify the trade-offs between the electromagnetic and mechanical performances of the motor.

In chapter [4] the analytical design concept is applied to given motor specifications and successively the machine design is analyzed by the finite elements software Flux2D by Altair in chapters [5] and [7]. The innovative "Machaon" rotor configuration is adopted in chapter [6] to compensate electromagnetic torque harmonics obtaining a smoother torque profile. The starting design assumptions are validated in the analysis step and the application requirements are satisfied by the design results. In particular the main performance advantages of synchronous reluctance machines are maintained and the main drawbacks are limited to

acceptable values. The final design exhibits an efficiency of 95% and a volumetric torque density of 10.5 $\frac{\mathrm{kNm}}{\mathrm{m}^3}$, which is an interesting value for the standards considering the motor size. The synchronous reluctance machines figure of merit is the saliency ratio ξ. The motor reaches a saliency ratio ξ value equal to 9.35, which is near to the optimum fixed to 10. At last the maximum power factor achievable $\cos(\varphi)$ is maximized to the value of 0.80 and the torque ripple Δ_T is reduced to 8.5%.

Contents

1 Introduction

Evident climatic changes and decreasing energetic resources have forced the worldwide society to reduce unavoidably greenhouse gases emission and environment pollution. According to the European Environment Agency, the European Union is achieving its greenhouse gases emission reduction target of 20% decrease within 2020 compared to 1990 levels (see fig.[1.1]).

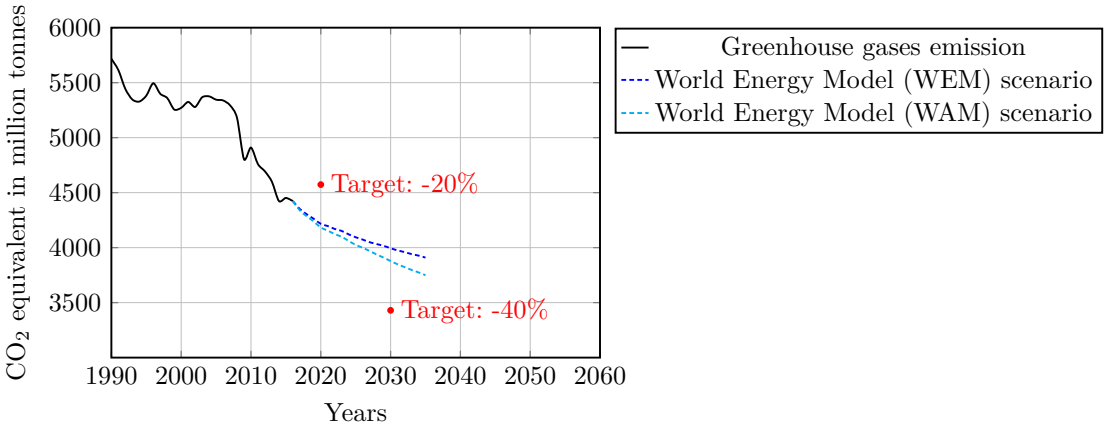

Figure 1.1 – Greenhouse gases emission trends, projections and targets in Europe [12]

Governments and institutions helped European countries to achieve their environmental targets in a profitable way by adopting energy policies consisting in regulations and funding. Not only the diversification of fossils fuels used and the structural changes in the economy made the decreasing trend possible. Indeed the renewable energy sources increase and the energy efficiency improvements contributed to reduce the environment pollution limiting harmful emissions.

In order to achieve the next environmental targets and the minimum final goal of -80% greenhouse gases emission decrease within 2050, the research and development of low environmental impact solutions should embrace every industrial sectors.

Greenhouse gases emissions decreased in the majority of industrial sectors with the notable exception of transport, as shown in fig.[1.2]. Manufacturing and construction industries remain one of the most polluting sector although accounted the largest CO_2 emissions decrease (-37%). Road transport, international aviation and shipping increased very rapidly during the 25-year period constituting a main cause of CO_2 emissions. In particular the road transport sector emissions increased of 16% and international aviation emissions even of 105%. Therefore, the transport sector electrification gained wide interest in order to limit the CO_2 emissions. Not only the road but also the air electrical mobility is investigated nowadays aiming to low environmental impact solutions generating as well economical profits for the

companies. Every engineering field is involved in developing different options to conventional mobility. In particular designing even more efficient electric machines is one of the engineering tasks to achieve environmental sustainable technologies.

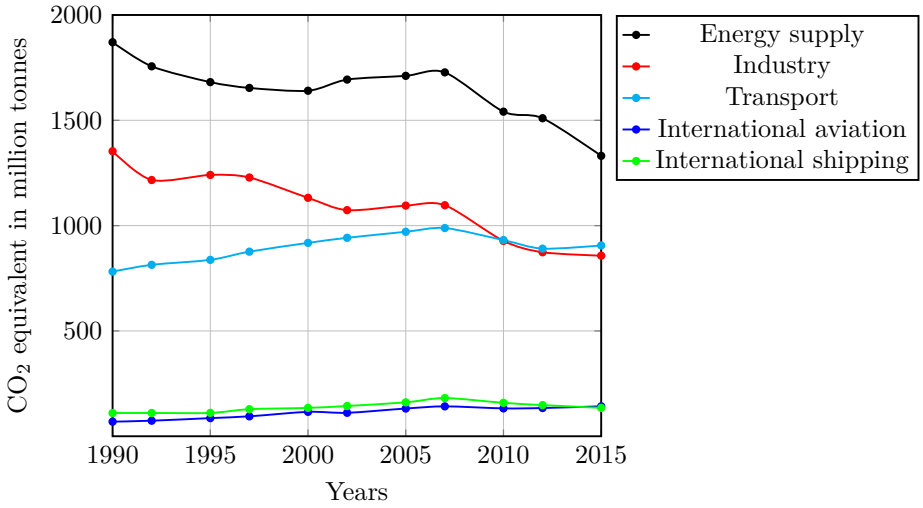

Figure 1.2 – CO_2 emissions by aggregated sector [13]

1.1 Road electrical mobility

Pure electric vehicles and hybrid electric vehicles are about to enter the mass market thanks to the rapid advances in technology and expected drop in the new models prices. The main causes of air quality problems in European cities are the emissions of carbon dioxide CO_2 and air pollutants like nitrogen oxides and particulate matter. Vehicles powered by electrical energy are much more energy efficient than those powered by internal combustion engines and also much less polluting. A widespread use of electric vehicles would lead to a reduction in greenhouse gases emission and to an improved air quality level in city centers and key transport sections. Electric vehicles powered by renewable energy sources could reduce greenhouse gases emissions by 80-95% within 2050 moving towards a low-carbon future [11].

In order to fully embrace electric mobility as soon as possible, the problems related to this technology must be faced up and solved. Consumers are not completely attracted by electric mobility due to several reasons:

- High starting costs
- Reliability
- Vehicle range expectancy
- Charging availability

Automotive manufacturers, energy providers and governments have already solved some of these problems but some of them remain. A European Environment Agency analysis suggests

that if the use of electric vehicles reaches 80% by 2050, an additional 150 GW of electric power supply should be necessary for charging them. Therefore, energy providers and governments must guarantee for the consumers the extra electric energy demand supplied by renewable sources to not undermine the electric mobility environment benefits. Furthermore, proper charging infrastructures and electric grid adjustments must be ensured.

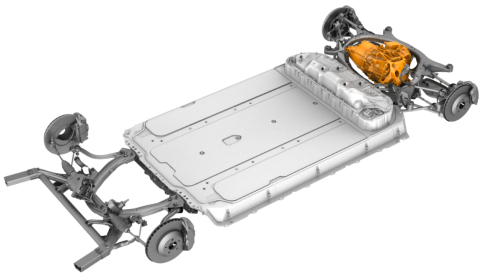

Figure 1.3 – Tesla Model 3 drive train [24]

Automotive manufacturers focus on different vehicle powertrain solutions in efficiency and cost saving terms (see fig.[1.3]). Batteries are one of the most important issue because they affect heavily the vehicle cost, reliability and range. Electric motor is the core of the vehicle powertrain and indeed traction system characteristics define the overall vehicle performances. The operating conditions of road transport applications are very demanding because they require frequent accelerations and regenerative braking that stress electromagnetically and mechanically the motor. The pure electric vehicles and hybrid electric vehicles powertrain is generally powered by synchronous electric motors equipped with permanent magnets (see fig.[1.4]).

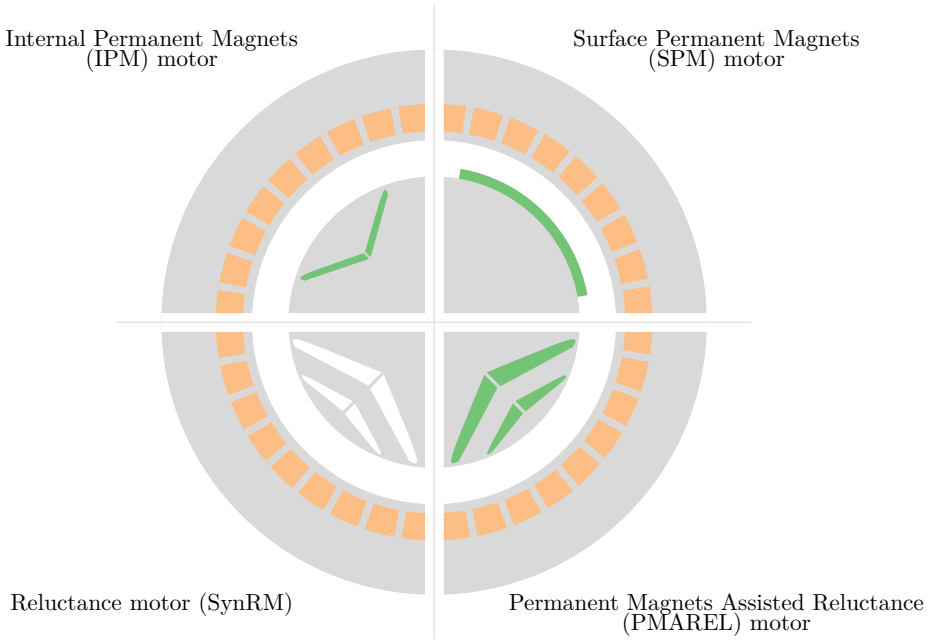

Figure 1.4 – Synchronous electric motors class

This electric motor class presents suitable features for these performance requirements. For example synchronous electric motors exhibit an high power and torque density, high efficiency and also wide constant power operating region. Nevertheless, the permanent magnets presence involves some disadvantages:

- High rare-earth permanent magnets costs
- Reliability due to permanent magnets demagnetization
- Temperature sensitivity
- Corrosives sensitivity
- Rare-earth provision for mass production

In automotive sector most of technological innovations are derived by motorsport. Indeed companies taking part of motorsport championships develop new technological solutions to improve their vehicle performances pushed by competitiveness. Also the electrical mobility technologies owe a lot to motorsport companies. The most emblematic example is the Formula E championship. The Formula E championship does not contribute only to technological development but also promotes around the world electrical mobility projects and ideas in order to help its spread. The racing cars taking part to the Formula E championship are pure electric vehicles powered by the McLaren E-Motor (see fig.[1.5]). Although this example clearly shows how consolidated this technology is and its results, exists the need to develop cost saving solutions that could be adopted on a large scale.

Figure 1.5 – Formula E 2019 car [15] and McLaren E-Motor [18]

McLaren E-Motor

McLaren is the single electric motors supplier in the Formula E championship. In this field the McLaren E-Motor represents the maximum technological expression in electrical and mechanical performances terms (see tab.[1.1]). The 120 kW E-motor is a surface permanent magnets synchronous motorgenerator primarily designed for electric and hybrid vehicles. An advance liquid cooling system and the small size allow the E-motor to achieve a power density value of 4.6 $\frac{\text{kW}}{\text{Kg}}$.

Table 1.1 – McLaren E-Motor features

Transient power = 120 kW
Transient torque = 130 Nm
Maximum speed = 17000 rpm
Efficiency = 96%
Nominal bus voltage = 545 V
Case diameter = 185 mm
Case length = 254 mm
Mass = 26 kg

1.2 Motivation

Taking into account the issues regarding electrical mobility explained in section [1.1], new solutions in efficiency and cost saving terms are deeply investigated in recent time. Synchronous reluctance motors have been re-considered in order to evaluate their competitiveness and to substitute them to synchronous permanent magnets motors for electric traction applications.

Synchronous reluctance motors present performance features similar to those of synchronous electric motors:

- Very high efficiency
- High torque density
- Wide flux weakening capability
- Wide overload capability
- High control dynamics and high speed stability in sensor-less electric drive

The unique rotor topology of synchronous reluctance motors guarantees electrical and mechanical advantages that lead to a longer service life and cost saving compared to synchronous motors class (see fig.[1.6]). In particular rare-earth permanent magnets and rotor winding copper costs are saved and furthermore, the consequent rotor winding absence ensures low operating temperature limiting losses and preserving motor service life. Accordingly, the main synchronous reluctance motors advantages respect to the competitors are:

- Cost saving
- Very high reliability
- Mechanical robustness
- Simple and robust in construction
- Simple maintenance
- Low operating temperature
- Inherently failure safe

- Large range of environmental operating conditions

Therefore, synchronous reluctance motors are perfectly suited for intermittent operating conditions and for severe demanding applications like the typical urban road vehicle traction characteristic. Nevertheless the complex rotor topology of the synchronous reluctance motors involves anyway some drawbacks:

- Low power factor
- High torque ripple

The most difficult design challenge is to obtain a low torque ripple adopting a proper rotor topology. Synchronous reluctance machines re-evaluation needs to a valid and strong design process. Generally hints derived from previous design experiences and fragmented studies are adopted to design synchronous reluctance machines. In this thesis a design concept based on analytical synchronous reluctance machine model is proposed. The analytical design concept could be used as starting basis to design synchronous reluctance machines for specific applications and requirements.

Figure 1.6 – Synchronous reluctance machine rotor topology [2]

2 Synchronous Reluctance Machines

In engineering field the aim of every machine design is to satisfy the required performances for given requirements and specifications. Due to the issue complexity, the design procedure is divided in a design or synthesis step and in an analysis step.

In the synthesis step, a simple and ductile model is analytically developed to achieve a main geometry and to satisfy the main performances of the machine. Then in the analysis step, a precise model is considered in order to obtain an optimal estimation of the behavior and machine characteristics. The main machine geometry is modified in its details to satisfy the required performances. Therefore, a deep understanding of the machine operating principles is an essential requisite to develop a valid and strong design concept.

In this chapter the electromagnetic torque generation of rotating electric machines is investigated and described through a simplified model. In particular a synchronous reluctance machine simplified model is analytically obtained and then adopted as starting point for the design process.

2.1 Synchronous reluctance machines class

Synchronous reluctance machines belong to the synchronous electric motors class. The mechanical angular speed of the rotor ω_{m} is therefore directly related to the stator winding supplying frequency f and to the rotor pole pairs number p:

$$\omega_{\mathrm{m}} = \frac{2\pi f}{p} \tag{2.1}$$

The laminated stator is isotropic and presents an AC distributed winding. The rotor does not present any rotor winding and permanent magnets but a distributed anisotropy introducing shaped air spaces called flux barriers, as shown in fig.[2.1].

Nowadays two different rotor configurations are considered thanks to their high efficiency:

- Transversely laminated anisotropic rotor
- Axial laminated anisotropic rotor

The transversely laminated anisotropic rotor configuration is investigated in this thesis because it presents evident industrial advantages in relatively cheap manufacture, easy construction and simple assembly terms compared to the axial laminated anisotropic rotor configuration.

Figure 2.1 – Transversely laminated synchronous reluctance machine [1]

2.2 Electromagnetic torque generation in synchronous electric machines

Consider the simplified model of a synchronous rotating electric machine composed of two coaxial solid cylinders with their respective reference systems (see fig.[2.15]).

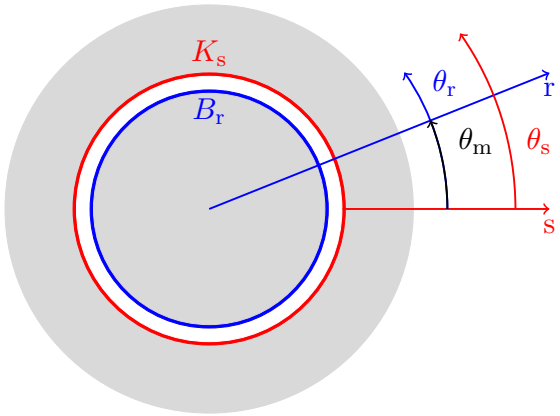

Figure 2.2 – Synchronous electric machine simplified model

The rotor is the inner cylinder and its reference system is fixed with respect to it. The rotor winding or permanent magnets create the flux density B_r along the airgap:

$$B_r(\theta_r) = \hat{B}_r \cdot \cos(\theta_r) \tag{2.2}$$

The flux density B_r presents its maximum value along the polar axis or d-axis. The stator is the outer cylinder and its reference system is fixed with respect to it. The stator winding creates a sinusoidal current distribution along the airgap called electrical loading K_s:

$$K_s(\theta_s) = \hat{K}_s \cdot \cos(\theta_s - \beta) \tag{2.3}$$

where β is the current phase displacement angle referring to the s-axis. From the relation $\theta_\mathrm{r} = \theta_\mathrm{s} - \theta_\mathrm{m}$, is it possible to express the equation (2.2) in the stator reference system:

$$B_\mathrm{r}(\theta_\mathrm{s}) = \hat{B}_\mathrm{r} \cdot \cos(\theta_\mathrm{s} - \theta_\mathrm{m}) \tag{2.4}$$

According to Lorentz force law, the interaction between the flux density B_r and the electrical loading K_s leads to an infinitesimal tangential force $dF(\theta_\mathrm{s})$ local production in each inner stator surface point:

$$dF(\theta_\mathrm{s}) = \left(\frac{DL}{2}\right) K_\mathrm{s}(\theta_\mathrm{s})\, B_\mathrm{r}(\theta_\mathrm{s})\, d\theta_\mathrm{s} \tag{2.5}$$

$$= \left(\frac{DL}{2}\right) \hat{K}_\mathrm{s} \cdot \cos(\theta_\mathrm{s} - \beta)\, \hat{B}_\mathrm{r} \cdot \cos(\theta_\mathrm{s} - \theta_\mathrm{m})\, d\theta_\mathrm{s} \tag{2.6}$$

where D and L are the inner stator diameter and the cylinders length respectively. Along the rotor surface an infinitesimal tangential force $-dF(\theta_\mathrm{s})$ is applied according to Newton's third dynamic law. The total tangential force F acting along the stator surface is:

$$F = \int_0^{2\pi} dF(\theta_\mathrm{s})\, d\theta_\mathrm{s} \tag{2.7}$$

$$= \left(\frac{DL}{2}\right) \hat{K}_\mathrm{s}\, \hat{B}_\mathrm{r} \int_0^{2\pi} \cos(\theta_\mathrm{s} - \beta) \cdot \cos(\theta_\mathrm{s} - \theta_\mathrm{m})\, d\theta_\mathrm{s} \tag{2.8}$$

$$= \left(\frac{DL}{2}\right) \hat{K}_\mathrm{s}\, \hat{B}_\mathrm{r}\, \frac{1}{2} \int_0^{2\pi} \cos(2\theta_\mathrm{s} - \beta - \theta_\mathrm{m}) + \cos(\theta_\mathrm{m} - \beta)\, d\theta_\mathrm{s} \tag{2.9}$$

having applied the Werner formula $\cos(\alpha) \cdot \cos(\beta) = \frac{1}{2}[\cos(\alpha + \beta) + \cos(\alpha - \beta)]$. Since the term:

$$\int_0^{2\pi} \cos(2\theta_\mathrm{s} - \beta - \theta_\mathrm{m})\, d\theta_\mathrm{s} = 0 \tag{2.10}$$

does not yield any contribution, the total tangential force F is expressed as:

$$F = \left(\frac{\pi DL}{2}\right) \hat{K}_\mathrm{s}\, \hat{B}_\mathrm{r} \cdot \cos(\theta_\mathrm{m} - \beta) \tag{2.11}$$

A fundamental parameter to evaluate the machine performances and also to compare different machines typologies is the electromagnetic torque T. The electromagnetic torque T acting on the rotor is therefore:

$$T = F \cdot \frac{D}{2} \tag{2.12}$$

$$= \left(\frac{\pi D^2 L}{4}\right) \hat{K}_\mathrm{s}\, \hat{B}_\mathrm{r} \cdot \cos(\theta_\mathrm{m} - \beta) \tag{2.13}$$

According to equation (2.13), the maximum electromagnetic torque value is obtained for $\theta_\mathrm{m} = \beta$ that is for the electrical loading K_s aligned to the flux density B_r:

$$T = \left(\frac{\pi D^2 L}{4}\right) \hat{K}_\mathrm{s}\, \hat{B}_\mathrm{r} \tag{2.14}$$

Consider a sinusoidal current distribution along the airgap K_s also depending on time:

$$K_\mathrm{s}\left(\theta_\mathrm{s}(t)\right) = \hat{K}_\mathrm{s} \cdot \cos\left(\theta_\mathrm{s}(t) - \beta\right) \tag{2.15}$$

where $\theta_\mathrm{s}(t) = \omega t$ and $\omega = 2\pi f$ is the sinusoidal current distribution angular speed function of the frequency f. According to equation (2.4) and to the maximum torque generation condition $\theta_\mathrm{m} = \beta$, the airgap flux density B_r could be expressed in the stator reference system:

$$B_\mathrm{r}\left(\theta_\mathrm{s}(t)\right) = \hat{B}_\mathrm{r} \cdot \cos\left(\theta_\mathrm{s}(t) - \beta\right) \tag{2.16}$$

Due to the torque applied, the rotor moves synchronously to the sinusoidal current distribution at the angular speed ω aligning its polar axis to the stator axis.

Concluding, the electromagnetic torque generation in synchronous electric machines is caused by the interaction between the stator K_s and rotor B_r electromagnetic fields and their respective phase displacement $\phi = \theta_\mathrm{m} - \beta$. In particular the rotor moves synchronously to the stator rotating magnetic field keeping the phase displacement ϕ constant. For fixed electrical loading $\hat{K}_\mathrm{s}$ and magnetic loading $\hat{B}_\mathrm{r}$, the torque value is proportional to the machine volume at the airgap $\left(\frac{\pi D^2 L}{4}\right)$ and therefore equation (2.14) could be adopted as starting design basis to size the machine [6].

2.3 Electromagnetic torque generation in synchronous reluctance machines

As explained in section [2.2], the electromagnetic torque generation in synchronous electric machines is caused by the interaction between the stator and rotor magnetic field. Due to the rotor winding and permanent magnets absence, in synchronous reluctance machines there is no rotor magnetic field. Therefore, equations based on Lorentz force law can not be applied directly to evaluate the electromagnetic torque.

The physical working principle of in synchronous reluctance machines is explained in energy W and co-energy W' terms. In section [2.3.1], the co-energy W' notion is mathematically introduced and then applied to evaluate the electromagnetic torque in sections [2.3.2] and [2.3.3].

2.3.1 Magnetic co-energy W'

The co-energy W' is a non physical quantity derived from the Lagrangian and Hamiltonian formulation for systems storing and transforming energy. In electromagnetic systems the magnetic energy W can be stored in electric field capacitance or in magnetic field inductance. Considering the constitutive equation, the energy density w stored in a non-linear electromagnetic system could be expressed in the plane (H,B) as:

$$B = \mu H \tag{2.17}$$

$$w = \int_0^B H \, dB \tag{2.18}$$

where H is the magnetic field, B is the magnetic flux density and μ is the medium magnetic permeability (see fig.[2.3]).

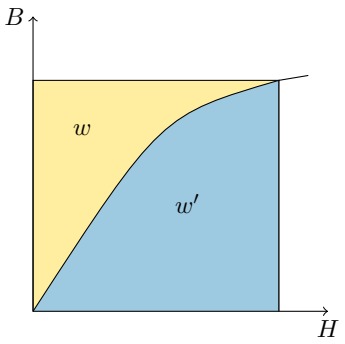

Figure 2.3 – Magnetic energy w and co-energy density w' in a non-linear electromagnetic system

According to Legendre transformation the co-energy density w' is defined as:

$$w' = \int_0^H B\, dH \tag{2.19}$$

It is possible to verify graphically from fig.[2.3] that the following relation is always valid:

$$w + w' = HB \tag{2.20}$$

Considering a linear electromagnetic system, the energy w and co-energy w' density are always equal (see fig.[2.4]):

$$w = w' \tag{2.21}$$

The co-energy W' notion is applied to explain and to evaluate the electromagnetic torque generation of a magnetic electromechanical system in section [2.3.2] and then of an elementary reluctance motor in paragraph [2.3.3] extending the analysis to a three-phase synchronous reluctance motor.

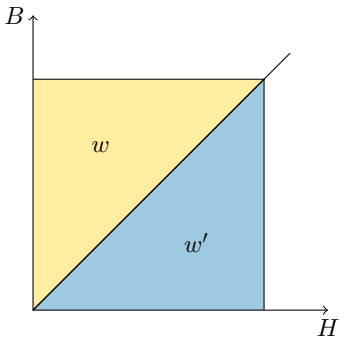

Figure 2.4 – Magnetic energy w and co-energy density w' in a linear electromagnetic system

2.3.2 Electromagnetic torque generation in a magnetic electromechanical system

Consider the following magnetic electromechanical system consisting of a fixed part and a rotating part characterized both by a magnetic permeability μ much greater than air magnetic permeability μ_0 shown in fig.[2.5]:

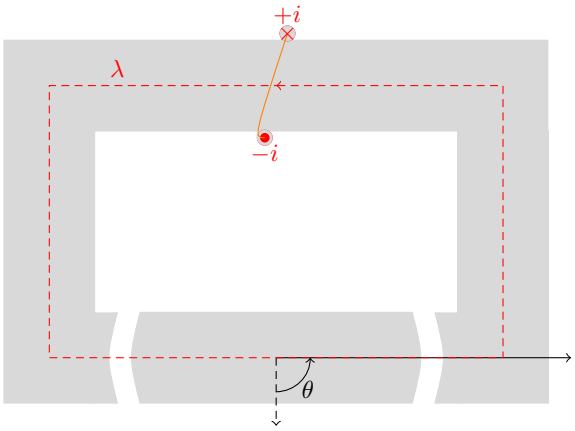

Figure 2.5 – Magnetic electromechanical system

Resistive, frictional and hysteresis losses are neglected and therefore, the magnetic field acting as a coupling field between the electrical and mechanical system, is conservative [20] [26]. The electrical system is described by the winding supplying current i and the by the linkage flux λ expressed according to Faraday-Neumann-Lenz law:

$$e = \frac{d\lambda}{dt} \tag{2.22}$$

where e is the induced voltage created by the magnetic field produced by the supplying winding current i. The mechanical system is described by the electromagnetic torque T acting at the mechanical angle θ.

According to the first law of thermodynamics and neglecting mechanical energy storage, in a lossless magnetic electromechanical system the balance of energy is expressed as:

$$W_{\mathrm{e}} = W + W_{\mathrm{m}} \tag{2.23}$$

where W_{e} is the electrical energy, W is the magnetic energy and W_{m} is the mechanical energy. Considering an infinitesimal dt and $d\theta$ variation, the differential balance of energy is:

$$vi\,dt = dW + T\,d\theta \tag{2.24}$$

Substituting equation (2.22) into the previous one, the differential magnetic energy dW is expressed in function of the linkage flux λ and the mechanical angle θ variation:

$$dW(\lambda,\theta) = i\,d\lambda - T\,d\theta \tag{2.25}$$

The stored magnetic energy W is consequently obtained as:

$$W(\lambda,\theta) = \int_0^{\theta}\int_0^{\lambda} [i\, d\lambda - T\, d\theta] \tag{2.26}$$

Being coupling field conservative, the magnetic energy W is a state function of the independent state variables λ and θ. The magnetic energy variation between any two points in the variables λ and θ is independent of the integration path allowing to consider any. Keeping the flux linkage λ at zero and rising the mechanical angle θ to its final value, the stored magnetic energy W is zero because the electromagnetic torque T is also zero. Therefore, equation (2.26) is integrated more conveniently rising mechanical angle θ to its final value:

$$W(\lambda,\theta) = \int_0^{\lambda} i(\lambda,\theta)\, d\lambda \tag{2.27}$$

The stored magnetic energy W is a single-valued state function of the independent state variables λ and θ. Considering the partial derivatives holding the other state variable constant, the differential stored magnetic energy $dW(\lambda,\theta)$ can be also expressed as:

$$dW(\lambda,\theta) = \frac{\partial W}{\partial \lambda} d\lambda + \frac{\partial W}{\partial \theta} d\theta \tag{2.28}$$

Being λ and θ independent variables, the previous equation is equal to equation (2.25). Equating the respective coefficient of $d\lambda$ and $d\theta$, it is possible to obtained the current i and the electromagnetic torque T from the partial derivative of the stored magnetic energy W using the flux linkage λ and the mechanical angle θ as independent variables:

$$i = \frac{\partial W(\lambda,\theta)}{\partial \lambda} \tag{2.29}$$

$$T = -\frac{\partial W(\lambda,\theta)}{\partial \theta} \tag{2.30}$$

The electromagnetic torque T is function of the stored magnetic energy W as shown by equation (2.30). In particular keeping the flux linkage λ constant, a stored magnetic energy W negative variation leads to a positive electromagnetic torque T generation (see fig.[2.6]).

The current i is a function of the linkage flux λ and the mechanical angle θ as shown by equation (2.29):

$$i = i(\lambda,\theta) \tag{2.31}$$

Therefore the flux linkage λ can be expressed as a function of the current i and the mechanical angle θ:

$$\lambda = \lambda(i,\theta) \tag{2.32}$$

The stored magnetic energy W is expressed by the independent state variables current i and mechanical angle θ:

$$W = W(i,\theta) \tag{2.33}$$

This independent state variables selection is more convenient form a practical point of view because the state variable current i is easily measured and controlled compared to the state

variable flux linkage λ. Considering an infinitesimal di and $d\theta$ variation, the differential magnetic energy $dW(i,\theta)$ is expressed as:

$$dW(i,\theta) = d(\lambda i) - \lambda\, di - T\, d\theta \tag{2.34}$$

having applied the differentiation rule to equation (2.25):

$$i\, d\lambda = d(\lambda i) - \lambda\, di \tag{2.35}$$

According to the Legendre transformation introduced in section [2.3.1], the differential magnetic co-energy $dW'(i,\theta)$ can be expressed as:

$$dW + dW' = d(\lambda i) \tag{2.36}$$

$$dW'(i,\theta) = \lambda\, di + T\, d\theta \tag{2.37}$$

The magnetic co-energy $W'(i,\theta)$ is obtained rising mechanical angle θ to its final value as already seen in equation (2.27):

$$W'(i,\theta) = \int_0^i \lambda(i,\theta)\, di \tag{2.38}$$

Considering the partial derivatives holding the other state variable constant, the differential magnetic co-energy $dW'(i,\theta)$ can be also expressed:

$$dW'(i,\theta) = \frac{\partial W'}{\partial i} di + \frac{\partial W'}{\partial \theta} d\theta \tag{2.39}$$

Equating the previous equation to equation (2.37), it is possible to obtain the flux linkage λ and the electromagnetic torque T from the partial derivative of the magnetic co-energy W' using the current i and mechanical angle θ as independent variables:

$$\lambda = \frac{\partial W'(i,\theta)}{\partial i} \tag{2.40}$$

$$T = \frac{\partial W'(i,\theta)}{\partial \theta} \tag{2.41}$$

The electromagnetic torque T is function of the magnetic co-energy W' as shown by the equation (2.41). In particular keeping the current i constant, a magnetic co-energy W' positive variation leads to a positive electromagnetic torque T generation (see fig.[2.6]).

The electromagnetic torque T can be expressed in stored magnetic energy $W(i,\theta)$ terms substituting equation (2.36) into equation (2.41); and in magnetic co-energy $W(\lambda,\theta)$ terms substituting equation (2.36) into equation (2.30):

$$T = i\frac{\partial \lambda(i,\theta)}{\partial \theta} - \frac{\partial W(i,\theta)}{\partial \theta} \tag{2.42}$$

$$T = \frac{\partial W'(\lambda,\theta)}{\partial \theta} - \lambda\frac{\partial i(\lambda,\theta)}{\partial \theta} \tag{2.43}$$

It is easy to verify graphically that equations (2.42) and (2.43) lead to the same conclusions already seen in fig.[2.6].

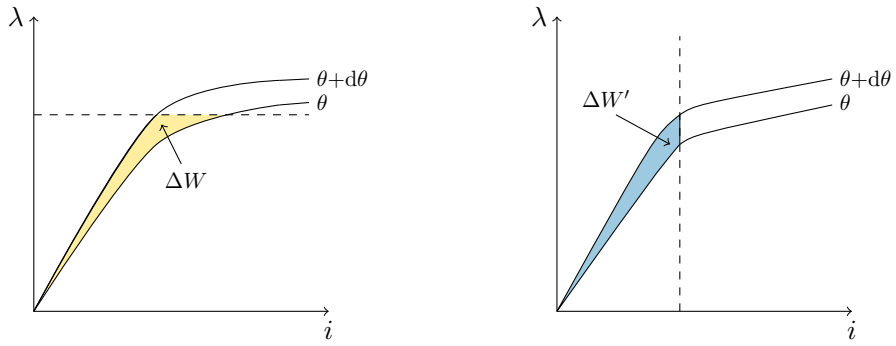

Figure 2.6 – Magnetic energy ΔW and magnetic co-energy variation $\Delta W'$ in a non-linear magnetic electromechanical system

Taking in to account that is possible to correlate the magnetic energy ΔW and co-energy $\Delta W'$ variation to electromagnetic torque T generation in a magnetic electromechanical system; the latter reaction to an electrical energy variation is investigated as it was an elementary motor supplied by a generic electric energy source. Consider a positive differential electrical energy variation dW_e:

$$dW_\mathrm{e} = vi\,dt \tag{2.44}$$

According to energy conservation law the following relation must be valid:

$$vi\,dt = i\,d\lambda \tag{2.45}$$

The differential energy balance can be also expressed as:

$$dW_\mathrm{e} = dW + dW_\mathrm{m} \tag{2.46}$$

$$i\,d\lambda = dW + T\,d\theta \tag{2.47}$$

This differential electrical energy variation dW_e can be represented graphically by the related operating points described in the (i,λ) plane by the coordinates (i_1, λ_1) at the generic mechanical angle θ and (i_1, λ_2) at the generic mechanical angle $\theta + d\theta$.

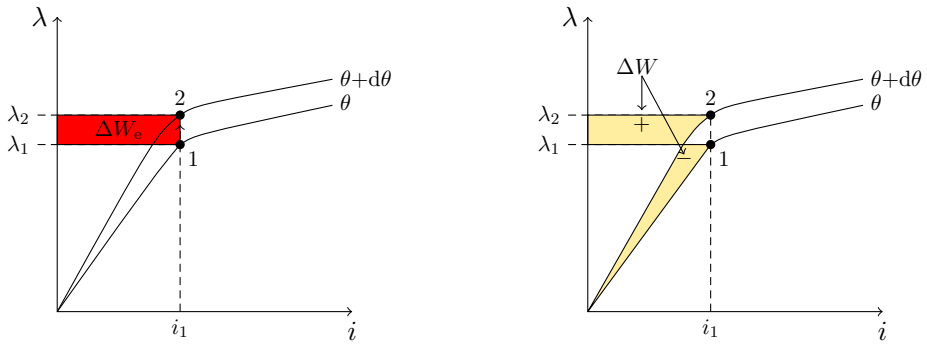

Figure 2.7 – Electrical energy ΔW_e and magnetic energy variation ΔW in a non-linear magnetic electromechanical system

In order to keep the energy balance unchanged, the magnetic electromechanical system converts the differential magnetic energy variation dW into differential mechanical energy

variation dW_{m} moving to an operating point described by the coordinates (i_1, λ_2) at the mechanical angle $\theta + d\theta$. The energy balance can be evaluated considering fig.[2.7]:

$$\int_{\lambda_1}^{\lambda_2} i\, d\lambda = \left(\int_{0}^{\lambda_2} i\, d\lambda - \int_{0}^{\lambda_1} i\, d\lambda \right) + T\, d\theta \tag{2.48}$$

$$(\lambda_2 - \lambda_1)\, i = W_2 - W_1 - \Delta W_{\mathrm{m}} \tag{2.49}$$

In order to increase the flux linkage λ according to the positive electrical energy variation ΔW_{e}, an electromagnetic torque T is applied to the rotating part of the magnetic electromechanical system aligning it to a privileged mechanical position $\theta + d\theta$ in flux linkage λ terms, as shown by equation (2.43). From fig.[2.6] and fig.[2.8] is graphically validated that the mechanical energy variation ΔW_{m} is equal to the magnetic co-energy variation $\Delta W'$.

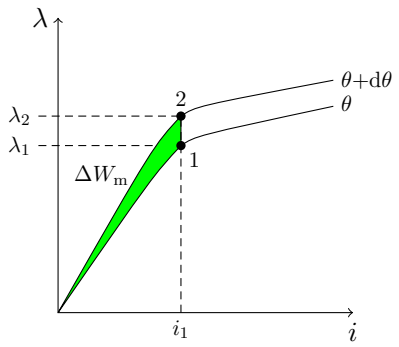

Figure 2.8 – Mechanical energy variation ΔW_{m} in a non-linear magnetic electromechanical system

Concluding, the magnetic electromechanical system increases its magnetic co-energy W' in order to keep the energy balance unchanged. From a physical point of view, it increases its flux linkage λ applying an electromagnetic torque T to its rotating part.

2.3.3 Electromagnetic torque generation in an elementary reluctance motor

According to the considerations shown in section [2.3.2] regarding the electromagnetic torque T generation, elementary reluctance motor electromagnetic torque T is now analytically expressed.

Consider the following elementary reluctance motor model shown in fig.[2.9]. The stator presents a N conductors distributed winding. The stator distributed winding is represented by an equivalent concentrated winding supplied by a sinusoidal current i:

$$i = \sqrt{2}\, I \cdot \sin(\omega_{\mathrm{e}} t) \tag{2.50}$$

where ω_{e} is the current electrical angular speed related to its frequency f. The stator winding magnetic axis x rotates synchronously to the current electrical angular speed ω_{e} along the airgap circumference. The anisotropic rotor, free to rotate on its shaft, is represented by an equivalent isotropic structure described by its mechanical angular position θ_{r} in the (d,q) system of reference. The d-axis represents the minimum reluctance axis characterized by the

airgap length g_d, while the q-axis the maximum reluctance axis characterized by the airgap length g_q.

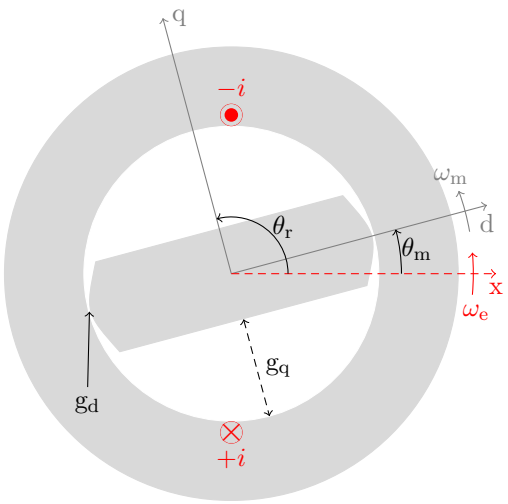

Figure 2.9 – Elementary reluctance motor

The sinusoidal current i creates a magnetic flux ϕ crossing the airgap and the rotor to re-close in to stator. According to Hopkinson law, it is possible to express the relation between the current i and the magnetic flux ϕ equating the magnetomotive force to the magnetic voltage drop:

$$N\,i = R\,\phi \tag{2.51}$$

where R is the magnetic circuit reluctance defined as:

$$R = \frac{l}{\mu\,S} \tag{2.52}$$

where μ is the medium magnetic permeability, l and S are the length and the normal section of the surface crossed by magnetic flux ϕ respectively. Substituting the flux linkage λ by the stator winding defined as:

$$\lambda = N\,\phi \tag{2.53}$$

and the inductance L defined as:

$$L = \frac{N^2}{R} \tag{2.54}$$

in equation (2.51), the relation between the current i and the flux linkage λ can be expressed as:

$$\lambda = L\,i \tag{2.55}$$

Neglecting leakage flux lines, every magnetic flux ϕ line crosses the normal section S and therefore the inductance L depends on the length l and on the magnetic permeability μ of the magnetic paths crossed by the magnetic flux ϕ lines:

$$\lambda = L(l,\mu)\,i \tag{2.56}$$

The rotor angular position θ_r determines the magnetic paths length in air g(d,q) and consequently the inductance L can be expressed in function on the rotor angular position θ_r:

$$\lambda = L(\theta_r)\, i \tag{2.57}$$

Consider the magnetic characteristics in the (i,λ) plane for different rotor angular position θ_r shown in fig.[2.10]:

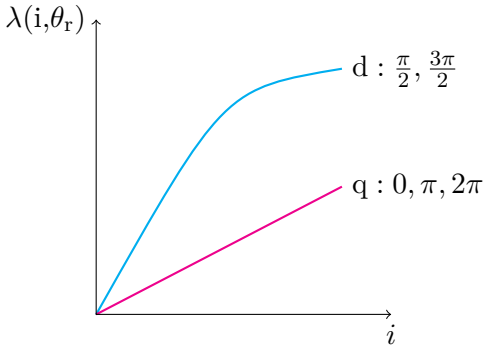

Figure 2.10 – Magnetic characteristics along q-axis and d-axis

For $\theta_r = 0, \pi, 2\pi$ the q-axis is aligned to the stator winding magnetic x-axis and the inductance along the q-axis L_q presents the lowest values due to the high airgap value along the q-axis g_q. Consequently the q-axis magnetic characteristic presents the lowest flux linkage λ_q values and it is proportional to the current i because large part of magnetic paths is in air and it is not affected by saturation effect. For $\theta_r = \frac{\pi}{2}, \frac{3\pi}{2}$ the d-axis is aligned to the stator winding magnetic x-axis and the inductance along the d-axis L_d presents the highest values due to the low airgap value along the d-axis g_d. Consequently the d-axis magnetic characteristic presents the highest flux linkage λ_d values and it is not proportional to the current i because most of magnetic paths is in iron and it is heavily affected by saturation (see fig.[2.11]).

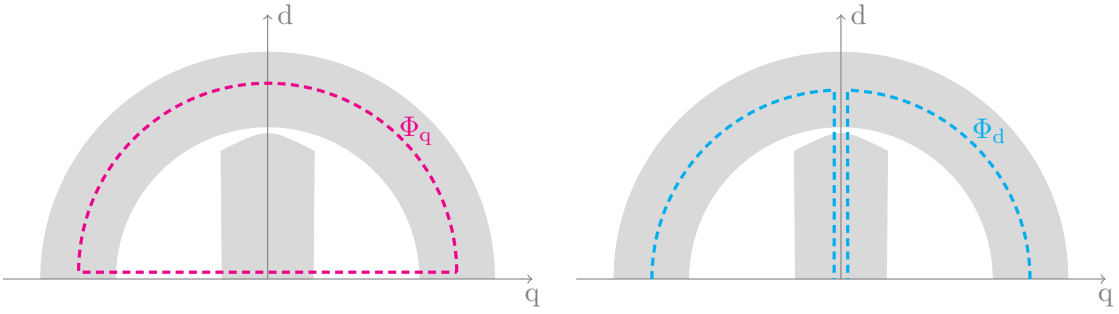

Figure 2.11 – Magnetic flux path along q-axis and d-axis

Assuming a sinusoidal variation of the rotor angular position θ_r and neglecting the saturation effect, the inductance $L(\theta_r)$ can be expressed in function of the rotor angular position θ_r [20]:

$$L(\theta_r) = L_0 - \hat{L} \cdot \cos(2\,\theta_r) \tag{2.58}$$

where L_0 and $\hat{L}$ are the mean value and the alternate value respectively:

$$L_0 = \frac{L_\mathrm{d} + L_\mathrm{q}}{2} \tag{2.59}$$

$$\hat{L} = \frac{L_\mathrm{d} - L_\mathrm{q}}{2} \tag{2.60}$$

According to equations (2.38) and (2.57), the magnetic co-energy W' can be expressed in function of the inductance $L(\theta_\mathrm{r})$:

$$W'(i,\theta) = \int_0^i \lambda(i,\theta)\, di = \int_0^i L(\theta_\mathrm{r})\, i\, di = \frac{1}{2} L(\theta_\mathrm{r})\, i^2 \tag{2.61}$$

Substituting equations (2.61) and (2.50) into equation (2.41), the electromagnetic torque T can be expressed in magnetic co-energy W' terms:

$$T = \frac{\partial W'(i,\theta_\mathrm{r})}{\partial \theta_\mathrm{r}} \tag{2.62}$$

$$= \frac{1}{2} \frac{dL(\theta_\mathrm{r})}{d\theta_\mathrm{r}}\, i^2 \tag{2.63}$$

$$= \frac{L_\mathrm{d} - L_\mathrm{q}}{2} \cdot \sin(2\theta_\mathrm{r})\, i^2 \tag{2.64}$$

$$= (L_\mathrm{d} - L_\mathrm{q}) \cdot \sin(2\theta_\mathrm{r}) \cdot \sin^2(\omega_\mathrm{e} t)\, I^2 \tag{2.65}$$

Expressing the rotor angular position θ_r as:

$$\theta_\mathrm{r} = \omega_\mathrm{m} t - \theta_\mathrm{m} \tag{2.66}$$

where ω_m and θ_m are the rotor mechanical angular speed and the mechanical phase displacement between the d-axis and x-axis at $t = 0$ respectively; the average electromagnetic torque T_avg is not null only if the rotor rotates synchronously to the stator current i:

$$\omega_\mathrm{e} = \omega_\mathrm{m} \tag{2.67}$$

Therefore, the average electromagnetic torque T_avg value is:

$$T_\mathrm{avg} = \frac{L_\mathrm{d} - L_\mathrm{q}}{4} \cdot \sin(2\theta_\mathrm{m})\, I^2 \tag{2.68}$$

For fixed current I value and mechanical phase displacement θ_m, the difference between the d-axis inductance L_d and the q-axis inductance L_q determines the electromagnetic torque T value. In an isotropic cylindrical rotor the electromagnetic torque T value is always equal to zero because the difference between L_d and L_q is null. The maximum electromagnetic torque T value is obtained when the d-axis is aligned to the stator winding magnetic x-axis. Furthermore, the electromagnetic torque T value does not depends on the current i sign.

As explained in secton [2.3.2], the elementary reluctance motor increases its magnetic co-energy W' applying an electromagnetic torque T to the rotor in order to align its minimum reluctance axis d to the stator winding magnetic axis x in response to a positive electrical energy variation ΔW_e. Since the stator winding magnetic axis x is rotating at the ω_e speed, the rotor moves synchronously to it at the $\frac{d\theta_\mathrm{r}}{dt} = \omega_\mathrm{m}$ speed generating an average electromagnetic

torque T_{avg} to the shaft.

Consider an elementary reluctance motor characterized by $n > 1$ stator equivalent concentrated winding. The supplying currents of the $n > 1$ equivalent stator concentrated winding $i_1, i_2 ... i_n$ are assumed a balanced, symmetrical and isofrequential n-tuple such that:

$$i_1 = \sqrt{2}\, I \cdot \sin(\omega_{\text{e}} t) \tag{2.69}$$

$$i_2 = \sqrt{2}\, I \cdot \sin(\omega_{\text{e}} t - \frac{2\,\pi}{n}) \tag{2.70}$$

$$i_n = \sqrt{2}\, I \cdot \sin(\omega_{\text{e}} t + \frac{2\,\pi}{n}) \tag{2.71}$$

Extending the previous analysis and relations to such multiply excited system, the electromagnetic torque T can be expressed as:

$$T = \frac{\partial W'(i_1, i_2 ... i_n, \theta_{\text{r}})}{\partial \theta_{\text{r}}} \tag{2.72}$$

A case of particular concern to electric machine design is the three-phase electric machine. The supplying currents of the $n = 3$ equivalent stator concentrated winding i_1, i_2 and i_3 are assumed a balanced, symmetrical and isofrequential 3-tuple such that:

$$i_1 = \sqrt{2}\, I \cdot \sin(\omega_{\text{e}} t) \tag{2.73}$$

$$i_2 = \sqrt{2}\, I \cdot \sin(\omega_{\text{e}} t - \frac{2\,\pi}{3}) \tag{2.74}$$

$$i_3 = \sqrt{2}\, I \cdot \sin(\omega_{\text{e}} t + \frac{2\,\pi}{3}) \tag{2.75}$$

The electromagnetic torque T can be expressed in function of the supplying currents and of the rotor angular position θ_{r}:

$$T = \frac{\partial W'(i_1, i_2, i_3, \theta_{\text{r}})}{\partial \theta_{\text{r}}} \tag{2.76}$$

The temporal and spatial superposition of the supplying currents produces a rotating magnetic field at the ω_{e} speed. Consequently the magnetic axis x of the rotating magnetic field rotates at the ω_{e} speed and, as already widely explained, the rotor moves synchronously to it at the $\frac{d\theta_{\text{r}}}{dt} = \omega_{\text{m}}$ speed generating an average electromagnetic torque T_{avg} to the shaft.

2.4 Electromagnetic torque evaluation in synchronous reluctance machines

As explained in section [2.2] the magnetic coupling between stator and rotor magnetic field generates electromagnetic torque. Equations based on Lorentz force law can not be applied to evaluate directly the synchronous reluctance machines electromagnetic torque according to section [2.3]. Nevertheless it is possible to express the rotor reaction to the stator magnetic field assuming a fictitious rotor winding that produces a fictitious magnetic field B_{r}. A simplified mathematical model is obtained to estimate the fictitious rotor magnetic field B_{r} and to express the synchronous reluctance machines electromagnetic torque as seen in section [2.2] for a synchronous electric machine [27]:

$$T = \left(\frac{\pi}{2} L D\right) \hat{\text{B}}_r\, p\, \hat{U}_{\text{s}} \cdot \sin(2\alpha_{\text{i}}^{\text{e}}) \tag{2.77}$$

The stator is represented by a slotless stator supplied with an equivalent sinusoidal current density J_s layer continuously distributed along the smooth inner surface. The rotor presents a distributed anisotropic structure such that the d-axis is the minimum reluctance axis and the q-axis the maximum reluctance axis due to the air flux barriers introduction (see fig.[2.12]).

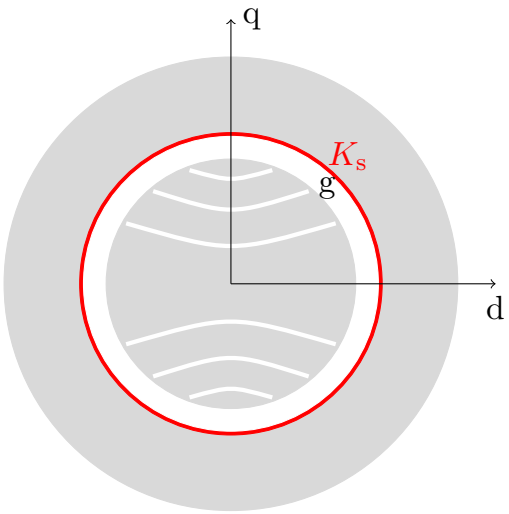

Figure 2.12 – Synchronous reluctance machine model

Consider the (d,q) system of reference synchronous with the rotor. The slotless stator creates a current density distribution along the airgap called electrical loading K_s. The electrical loading projections along the dq-axes are:

$$\hat{K}_s^d = \hat{K}_s \cdot \cos(\alpha_i^e) \tag{2.78}$$

$$\hat{K}_s^q = \hat{K}_s \cdot \sin(\alpha_i^e) \tag{2.79}$$

where α_i^e is the displacement angle between the electrical loading K_s and its projection on the d-axis K_s^d. The stator electrical loading K_s produces along the airgap the stator scalar magnetic potential U_s. The stator scalar magnetic potential U_s is the stator magnetomotive force distribution along the airgap and according to Ampere's law it is expressed as:

$$U_s = \int_0^{\pi} K_s \frac{D}{2} d\theta^e \tag{2.80}$$

Therefore, the current density distribution waveform is 90 electrical degrees leading the magnetic field distribution waveform. The stator scalar magnetic potential U_s components on d-axis and q-axis are respectively:

$$\hat{U}_s^d = \frac{D\,\hat{K}_s^d}{2p} \tag{2.81}$$

$$\hat{U}_s^q = \frac{D\,\hat{K}_s^q}{2p} \tag{2.82}$$

Consequently the airgap flux density due to the stator B_s components are:

$$\hat{B}_s^d = \frac{\mu_0 \hat{U}_s^d}{g} \tag{2.83}$$

$$\hat{B}_s^q = \frac{\mu_0 \hat{U}_s^q}{g} \tag{2.84}$$

Due to its topology, the rotor reacts to the stator scalar magnetic potential U_s distorting B_s waveform and creating a different airgap flux density waveform B_g. Neglecting cross-coupling effect, the rotor reaction to the stator scalar magnetic potential U_s could be predict separately along the d-axis and the q-axis estimating the resultant airgap flux density waveform B_g. Indeed the stator magnetic potential along the d-axis U_s^d crosses high permeance magnetic paths and consequently it is not deformed by the rotor topology, instead the stator magnetic potential along the q-axis U_s^q crosses high reluctance magnetic paths and consequently it is heavily deformed by the rotor topology.

Figure 2.13 – The d-axis and q-axis equivalent model

Assuming g_d the equivalent magnetic airgap along the maximum permeance axis and g_q the equivalent magnetic air gap along the maximum reluctance axis, the rotor distorting effect on the airgap flux density due to the stator B_s could be estimated assuming an isotropic rotor with a fictitious scalar magnetic potential U_r and a fictitious airgap flux density B_r such that B_g is a linear superposition of B_s and B_r:

$$\hat{B}_g^d = \hat{B}_s^d + \hat{B}_r^d \tag{2.85}$$

$$\hat{B}_g^q = \hat{B}_s^d + \hat{B}_r^q \tag{2.86}$$

Having neglected cross-coupling effect, a d-axis and a q-axis equivalent model is considered to evaluate separately the U_r contributions along the dq-axes, as shown in fig.[2.13]. The electrical displacement angle α_i^e between the d-axis and q-axis stator scalar magnetic potential components U_s is assumed equal to 45° without loosing any general validity.

The equivalent magnetic airgap length along the d-axis g_d is greater than the actual airgap length g due to slot openings effect in the inner stator surface and to a physiological saturation. These effects are quantifiable taking in to account the Carter coefficient K_c and the d-axis saturation coefficient K_{sat}^d:

$$g_d = g\, K_c\, K_{sat}^d \tag{2.87}$$

In particular the Carter coefficient K_c evaluates the slots openings effect on the flux lines that cross the airgap. The slot openings lead to a non uniform airgap width and consequently to a flux lines deformation. The d-axis saturation coefficient K_{sat}^{d} is defined as the ratio between the magnetomotive force necessary to magnetize the whole machine along the d-axis and the magnetomotive force necessary to magnetize the airgap. From a magnetic point of view, the saturated iron paths behave as they were air and the d-axis saturation coefficient K_{sat}^{d} rates their effect on the d-axis magnetomotive force component and accordingly on the stator scalar magnetic potential U_s^d. The equivalent magnetic airgap length along the q-axis g_q is much greater than the actual airgap length g due to the total flux barriers thickness τ_b. Indeed the q-axis saturation coefficient K_{sat}^{q} accounts the magnetomotive force necessary to magnetize the whole machine along the q-axis and then it is heavily affected by the flux barriers air paths:

$$g_q = g\, K_c\, K_{sat}^{q} \tag{2.88}$$

Therefore, the fictitious rotor scalar magnetic potential along the q-axis U_r^q compensates almost entirely the stator scalar magnetic potential U_s^q, while the fictitious rotor scalar magnetic potential along the d-axis U_r^d is a fraction of U_s^d, as shown in fig.[2.14]:

$$\hat{U}_r^d = \hat{U}_s^d \left(\frac{g}{g_d} - 1\right) \tag{2.89}$$

$$\hat{U}_r^q = \hat{U}_s^q \left(\frac{g}{g_q} - 1\right) \tag{2.90}$$

Figure 2.14 – The d-axis and q-axis fictitious rotor scalar magnetic potential

These results find a physical validation because, as said before, the rotor substantially does not react along the q-axis due to the equivalent magnetic airgap g_q high value, instead it reacts along the d-axis accounting the slot openings effect and the saturation effect. Finally it is possible to estimate the fictitious airgap flux density B_r due to the rotor reaction considering the actual airgap length g and to express the electromagnetic torque T according to equation (2.77) (see fig.[2.15]):

$$\hat{B}_r^d = \frac{\mu_0\, \hat{U}_r^d}{g} \tag{2.91}$$

$$\hat{B}_r^q = \frac{\mu_0\, \hat{U}_r^q}{g} \tag{2.92}$$

$$\hat{B}_r = \sqrt{(\hat{B}_r^d)^2 + (\hat{B}_r^q)^2} \tag{2.93}$$

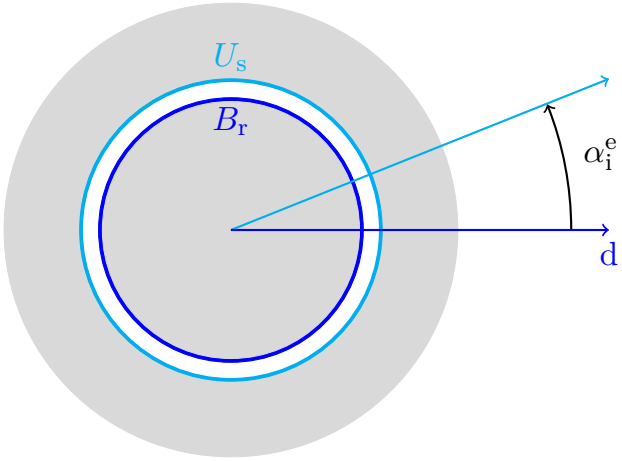

Figure 2.15 – Synchronous reluctance machine simplified equivalent model

3 Synchronous Reluctance Machines Analytical Design Concept

Considering the electromagnetic torque evaluation presented in section [2.4] and geometrical constrains regarding the application requirements, a preliminary machine sizing is obtained. The main machine dimensions are estimated assuming a stator magnetomotive force distribution U_{s} and a fictitious rotor flux density B_{r}. Subsequently, the stator and rotor geometry are designed and in particular the rotor geometry design is deeply investigated. Furthermore, the mechanical aspects are considered during the design process due to their important effects on the motor electromagnetic performances.

The machine requirements are:

- Nominal power P_{n}
- Synchronous speed n_{n}
- Number of phases $m = 3$
- Nominal voltage V_{n}

Generally the synchronous reluctance machines are designed for applications that require or operate with a three-phase system. Therefore, this configuration is investigated without losing any generality or validity regarding the design results.

Before to illustrate the design procedure in section [3.2], design aims and more considerations for a proper design are introduced in paragraph [3.1].

3.1 Saliency ratio ξ

Considering the (d,q) system of reference synchronous with the rotor it is possible to define the inductances along the d-axis L_{d} and along the q-axis L_{q}:

$$L_{\mathrm{d}} = L_{\mathrm{m}}^{\mathrm{d}} + L_{\delta} \tag{3.1}$$
$$L_{\mathrm{q}} = L_{\mathrm{m}}^{\mathrm{q}} + L_{\delta} \tag{3.2}$$

where L_{m} is the magnetizing inductance and L_{δ} is the stator leakage inductance. The stator leakage inductance L_{δ} is related to the leakage flux lines that cross magnetic paths only in the stator geometry and to the leakage flux lines that cross the airgap and link the rotor geometry.

The synchronous reluctance machines figures of merit are the saliency ratio ξ and the magnetizing saliency ratio ξ_{m}:

$$\xi = \frac{L_{\mathrm{d}}}{L_{\mathrm{q}}} = \frac{L_{\mathrm{m}}^{\mathrm{d}} + L_{\delta}}{L_{\mathrm{m}}^{\mathrm{q}} + L_{\delta}} \tag{3.3}$$

$$\xi_m = \frac{L_{\mathrm{m}}^{\mathrm{d}}}{L_{\mathrm{m}}^{\mathrm{q}}} \tag{3.4}$$

The overall electromagnetic performances of the machine are directly proportional to the saliency ratio ξ and it is adopted to evaluate the machine characteristics [22] [5]. The saliency ratio ξ depends on the stator and rotor topology and therefore the electromagnetic performances of the machine are heavily related to the mechanical design aspects. For a fixed magnetizing saliency ratio ξ_{m}, the stator leakage inductance L_{δ} increase leads to a saliency ratio ξ decrease and consequently to a machine performances worsening. The stator scalar magnetic potential temporal and spatial harmonics are related to the stator leakage inductance L_{δ} and they do not lead to any benefit in term of torque density, torque ripple and efficiency. Therefore, to achieve the maximum saliency ratio ξ, the magnetizing saliency ratio ξ_{m} has to be maximize and the stator leakage inductance L_{δ} has to be limited.

3.1.1 The d-axis linkage flux component Λ_{d} maximization

The main design objective is to maximize the average torque value finding the optimum magnetizing saliency ratio ξ_{m}. This ratio is related to the total iron islands τ_{i} thickness and the total flux barriers thickness τ_{b}. Indeed helping the d-axis flux component Φ_{d} circulation and obstructing the q-axis flux component Φ_{q} circulation, the average torque value increases.

Considering the linkage flux Λ by the stator winding, for fixed d-axis current component I_{d} and q-axis current component I_{q}, the magnetizing inductances L_{m} along the d-axis and q-axis have to be maximize and minimize respectively:

$$\Lambda_{\mathrm{d}} = L_{\mathrm{m}}^{\mathrm{d}} \cdot I_{\mathrm{d}} \tag{3.5}$$

$$\Lambda_{\mathrm{q}} = L_{\mathrm{m}}^{\mathrm{q}} \cdot I_{\mathrm{q}} \tag{3.6}$$

The d-axis stator scalar magnetic potential $U_{\mathrm{s}}^{\mathrm{d}}$ leads to the $L_{\mathrm{m}}^{\mathrm{d}}$ inductance which is equivalent, for a given airgap, to the magnetizing inductance of an induction motor [6]:

$$L_{\mathrm{m}}^{\mathrm{d}} = \frac{3}{\pi}\,\mu_0 \left(\frac{K_{\mathrm{w}}\,N_{\mathrm{s}}}{2p}\right)^2 \frac{D_{\mathrm{s,i}}\,L_{\mathrm{stk}}}{\mathrm{g_d}} \tag{3.7}$$

where K_{w} and N_{s} are the fundamental winding coefficient and the total number of equivalent series conductors respectively. According to equation (3.7), a low number of pole pairs p is recommended to increase the magnetizing inductance $L_{\mathrm{m}}^{\mathrm{d}}$:

$$2 \leq p \leq 3 \tag{3.8}$$

Furthermore, the airgap has to be kept as small as possible in order to increase the average torque according to mechanical constrains:

$$0.25 \leq \mathrm{g} \leq 0.5\,\mathrm{mm} \tag{3.9}$$

Intuitively the torque ripple is inversely proportional to the airgap value. The stator winding disposition has to be design to achieve the maximum fundamental winding coefficient K_{w} as explained in the following paragraph (3.1.2).

3.1.2 Temporal and spatial harmonics compensation

The most significant drawback of synchronous reluctance machines is the high torque ripple caused by the interaction between the stator scalar magnetic potential temporal harmonics $(U_{\mathrm{s}})_{\nu}$ and the rotor permeance variations that generates high order spatial harmonics in the rotor scalar magnetic potential U_{r}. Therefore, proper geometrical solutions have to be adopted in order to reduce as much as possible these phenomena related to the stator leakage inductances L_{δ} and to the rotor topology.

To prevent scalar magnetic potential temporal harmonics $(U_{\mathrm{s}})_{\nu}$ the stator winding has to be designed in order to produce a sinusoidal distributed scalar magnetic potential $(U_{\mathrm{s}})_1$ along the airgap.

An advantageous choice is adopting an AC double layer distributed winding with star connection to avoid the multiple of three temporal harmonics [6]. This solution leads to a lower stator slot leakage inductance $L_{\delta,\mathrm{slot}}$ and also to a shorter winding. Consequently the end winding leakage inductance $L_{\delta,\mathrm{ew}}$ and the Joule losses decrease improving the motor saliency ratio ξ and efficiency η. Furthermore, the fault tolerant machine capability is increased thanks to the physical separation between the phases. At last the copper winding and the total machine cost are reduced.

Selecting a proper number of stator slots per pole and per phase $q > 1$ and an optimal chording angle $\beta_{\mathrm{c}}^{\mathrm{e}}$ for a fixed electrical slot pitch $\alpha_{\mathrm{s}}^{\mathrm{e}}$ the fundamental winding factor $(K_{\mathrm{w}})_1$ is maximized reducing the scalar magnetic potential harmonic content. This coefficient allows to consider the distributed chorded winding as an equivalent one-conductor winding concentrated in a single point. In particular the fundamental winding factor $(K_{\mathrm{w}})_1$ is defined as:

$$(K_{\mathrm{w}})_1 = (K_{\mathrm{d}})_1 \cdot (K_{\mathrm{p}})_1 \tag{3.10}$$

where $(K_{\mathrm{d}})_1$ is the fundamental distribution factor, that accounts the winding distribution on q slots:

$$(K_{\mathrm{d}})_1 = \frac{\sin\left(q\frac{\alpha_{\mathrm{s}}^{\mathrm{e}}}{2}\right)}{q\sin\left(\frac{\alpha_{\mathrm{s}}^{\mathrm{e}}}{2}\right)} \tag{3.11}$$

and $(K_{\mathrm{p}})_1$ is the fundamental pitch factor, that accounts the layer shift on the other one:

$$(K_{\mathrm{p}})_1 = \cos\left(\frac{\beta_{\mathrm{c}}^{\mathrm{e}}}{2}\right) \tag{3.12}$$

The slot harmonics can not be compensated adopting a proper winding arrangement. Their order is expressed as:

$$\nu_{\mathrm{slot}} = k \cdot Q_{\mathrm{s}} \pm p \tag{3.13}$$

where k is an integer number.

The high order spatial harmonics in the rotor scalar magnetic potential U_r caused by the slot harmonics and the rotor topology are compensated adopting proper geometrical solutions in the rotor. In particular the flux barriers shape and their position involve the high order spatial harmonics generation. These constructive solutions are investigated in detail in section [3.4].

3.2 Design procedure

The adopted design concept consists in assuming a proper airgap flux density peak value $\hat{B}_\mathrm{g}$ to obtain the stator scalar magnetic potential U_s and to estimate the rotor reaction through its fictitious airgap flux density B_r.

According to equation (2.85), the stator scalar magnetic potential along the d-axis $\hat{U}_\mathrm{s}^\mathrm{d}$ is computed as:

$$\hat{U}_\mathrm{s}^\mathrm{d} = \frac{\mathrm{g_d}\,\hat{B}_\mathrm{g}^\mathrm{d}}{\mu_0} \tag{3.14}$$

The Carter coefficient K_c takes into account the slotting effect caused by the stator and rotor slots. As explained in section [3.4.1], the completely saturated rotor iron ribs could be considered magnetically as equivalent rotor slots and consequently they lead to an airgap flux density deformation. Furthermore, the d-axis saturation coefficient $K_\mathrm{sat}^\mathrm{d}$ has to be consider carefully due to the small airgap value g and to the high saturation operating conditions. Therefore, it is not possible predicting exactly the value of the d-axis equivalent magnetic airgap $\mathrm{g_d}$. As first design assumption, the d-axis equivalent magnetic airgap $\mathrm{g_d}$ is selected according to the following relation [6]:

$$1.2 \leq \frac{\mathrm{g_d}}{\mathrm{g}} \leq 1.6 \tag{3.15}$$

The stator scalar magnetic potential along the q-axis $\hat{U}_\mathrm{s}^\mathrm{q}$ is obtained from $\alpha_\mathrm{i}^\mathrm{e}$ and consequently $\hat{U}_\mathrm{s}$ is achieved:

$$\hat{U}_\mathrm{s}^\mathrm{q} = \hat{U}_\mathrm{s}^\mathrm{d} \cdot \tan(\alpha_\mathrm{i}^\mathrm{e}) \tag{3.16}$$

$$\hat{U}_\mathrm{s} = \sqrt{(\hat{U}_\mathrm{s}^\mathrm{d})^2 + (\hat{U}_\mathrm{s}^\mathrm{q})^2} \tag{3.17}$$

In order to maximize the torque density, defined as the ratio between the average torque value and the whole machine mass, the magnetizing current I_d and the torque current I_q have to be limited and maximize respectively for a fixed current nominal value I_n:

$$I_\mathrm{n} = \sqrt{(I_\mathrm{d})^2 + (I_\mathrm{q})^2} \tag{3.18}$$

Consequently the displacement angle $\alpha_\mathrm{i}^\mathrm{e}$ between the nominal current I_n and the magnetizing current I_d has to be selected greater than 45° leading to unbalanced current components along the dq-axes. Generally in synchronous reluctance machines the maximum torque per ampere (MTPA) conditions are obtained for $\alpha_\mathrm{i}^\mathrm{e}$ nearly to 65° [10]. Also according to equations (3.5) and (3.6) this unbalanced current components condition results convenient for high torque density achievement.

From equations (2.89) and (2.90) it is possible to estimate the fictitious rotor scalar magnetic potential $\hat{U}_\mathrm{r}$ and consequently, from equations (2.91) and (2.92) the fictitious airgap flux density due to the rotor $\hat{B}_\mathrm{r}$ as:

$$\hat{B}_\mathrm{r} = \mu_0 \frac{\hat{U}_\mathrm{s}}{2\mathrm{g_d}} \left(1 - \frac{\mathrm{g_d}}{\mathrm{g_q}}\right) \tag{3.19}$$

The equivalent magnetic airgap along the q-axis $\mathrm{g_q}$ is assumed much grater than the equivalent magnetic airgap along the d-axis $\mathrm{g_d}$ and therefore equation (3.19) becomes:

$$\hat{B}_\mathrm{r} = \mu_0 \frac{\hat{U}_\mathrm{s}}{2g_d} \tag{3.20}$$

Hence the main machine dimensions can be obtained according to equation (2.77):

$$L_\mathrm{stk}\, D_\mathrm{s,i} = \frac{2\, T_\mathrm{n}}{\pi\, \hat{B}_\mathrm{r}\, p\, \hat{U}_\mathrm{s} \cdot \sin(2\alpha_\mathrm{i}^\mathrm{e})} \tag{3.21}$$

The relation between the stack length L_stk and the stator inner diameter $D_\mathrm{s,i}$ could be fixed from geometrical application constrains such as maximum available length or maximum outer space. For a fixed external stator diameter, short machines exhibit a higher torque and power densities than long machines but lower power factor and efficiency.

3.2.1 Electrical parameters estimation

Fixing the machine efficiency η and the displacement angle φ between the nominal current I_n and the winding voltage V_w, it is possible to estimate the nominal current I_n:

$$I_\mathrm{n} = \frac{P_\mathrm{n}}{3\, V_\mathrm{w}\, \eta \cdot \cos(\varphi)}\,\mathrm{A} \tag{3.22}$$

Synchronous reluctance machines efficiency η is estimated from the same size, speed and output power induction machines efficiency η_im. As opposed to induction machines, in synchronous reluctance machines the Joule losses are localized only in the stator winding thanks to the rotor winding absence and consequently an efficiency improvement Δ_η is expected [19]. This efficiency improvement Δ_η respect to induction machines could be estimated as:

$$\Delta_\eta = \frac{100 - \eta_\mathrm{im}}{3} \tag{3.23}$$

Therefore, the efficiency η starting design assumption is:

$$\eta = \eta_\mathrm{im} + \Delta_\eta \tag{3.24}$$

The maximum achievable power factor $\cos(\varphi)$ in synchronous reluctance machines is function of the saliency ratio ξ [22]:

$$\cos(\varphi) = \frac{\xi - 1}{1 + \xi} \tag{3.25}$$

A reasonable saliency ratio is $\xi = 10$ and consequently a power factor $\cos(\varphi) = 0.8$ is a proper starting design assumption.

Having adopted an AC double layer distributed winding the number of equivalent series conductors per slot n_{cs} has to be integer and even [6]:

$$n_{\mathrm{cs}} = \frac{\pi \hat{U}_{\mathrm{s}}^{\mathrm{d}}}{3K_{\mathrm{w}}\, q\, \hat{I}_{\mathrm{d}}} \tag{3.26}$$

According to the parallel paths n_{pp} chosen, the actual number of conductors per phase N and per slot n_{c}, are:

$$N = n_{\mathrm{pp}}\, N_{\mathrm{s}} \tag{3.27}$$

$$n_c = n_{\mathrm{pp}}\, n_{\mathrm{cs}} \tag{3.28}$$

where $N_{\mathrm{s}} = \frac{n_{\mathrm{cs}} Q_{\mathrm{s}}}{m}$ is the number of equivalent series conductors per phase. Assuming an inner voltage drop of 0.5%, the winding voltage V_{w} is:

$$V_{\mathrm{w}} = 0.95 \frac{V_{\mathrm{n}}}{\sqrt{3}} \tag{3.29}$$

Finally it is possible to estimate the flux per pole $\hat{\Phi}$:

$$\hat{\Phi} = \frac{\sqrt{2}\, V_{\mathrm{w}}}{\pi\, K_{\mathrm{w}}\, f_{\mathrm{n}}\, N_{\mathrm{s}}} \tag{3.30}$$

3.3 Stator geometry

From the winding design considerations explained in section [3.1.2] and the dimensional and electrical estimations presented in section [3.2] a preliminary main stator geometry is achieved [6]. Obviously a more detailed stator design is required to complete entirely the machine design but in this study only a preliminary main stator geometry is considered to investigate deeply the rotor topology due to its fundamental influence on the machine performances. It is also possible to adopt a proper existing induction machine stator lamination.

Selecting a trapezoidal slot, in accordance with Gauss' law, the stator tooth width w_{t} is estimated assuming to not saturate its magnetic path and therefore hypothesizing a proper flux density peak value in the stator tooth $\hat{B}_{\mathrm{t}}$:

$$w_{\mathrm{t}} = \frac{\hat{B}_{\mathrm{g}}}{\hat{B}_{\mathrm{t}}} \frac{1}{K_{\mathrm{pack}}}\, p_{\mathrm{s}} \tag{3.31}$$

where $p_{\mathrm{s}} = \frac{\pi D_{\mathrm{s,i}}}{Q_{\mathrm{s}}}$ is the slot pitch and K_{pack} the packaging coefficient. Consequently the inner slot width $w_{\mathrm{w,i}}$ is:

$$w_{\mathrm{s,i}} = p_{\mathrm{s}} - w_{\mathrm{t}} \tag{3.32}$$

The slot cross section area S_{slot} is obtained fixing a current density $\hat{J}_{\mathrm{s}}$ value:

$$S_{\mathrm{slot}} = \frac{n_{\mathrm{cs}}\, \hat{I}_{\mathrm{n}}}{K_{\mathrm{fill}}\, \hat{J}_{\mathrm{s}}} \tag{3.33}$$

where K_{fill} is the filling coefficient and it is defined as the ratio between the actual conductors cross section area in the slot and the whole slot cross section area taking in to account the taken cross section area by the insulating material. For synchronous reluctance machines a standard current density value is $\hat{J}_{\text{s}} = 10\,\frac{\text{A}}{\text{mm}^2}$ but obviously it depends on the cooling system effectiveness and on the machine size [23].

Assuming a slot height h_{s} not greater than three times the inner slot width $w_{\text{s,i}}$ in order to limit the stator slot leakage inductances $L_{\delta,\text{slot}}$; the external slot width $w_{\text{s,e}}$ is obtained:

$$w_{\text{s,e}} = \left(\frac{2\,S_{\text{slot}}}{h_{\text{s}}} - w_{\text{s,i}}\right)\,\text{m} \tag{3.34}$$

The stator backiron height h_{bi} is calculated to not saturate its magnetic path assuming a proper flux density peak value in the stator backiron $\hat{B}_{\text{bi}}$. The magnetic flux that crosses the backiron surface $\hat{\Phi}_{\text{bi}}$ is a half of the flux per pole $\hat{\Phi}$:

$$\hat{\Phi}_{\text{bi}} = \frac{\hat{\Phi}}{2} \tag{3.35}$$

$$h_{\text{bi}} = \frac{\hat{\Phi}_{\text{bi}}}{\hat{B}_{\text{bi}}\,L_{\text{stk}}\,K_{\text{pack}}} \tag{3.36}$$

From the internal diameter $D_{\text{s,i}}$, the slot height h_{s} and the stator backiron height h_{bi} it is possible to calculate the external stator diameter $D_{\text{s,e}}$:

$$D_{\text{s,e}} = D_{\text{s,i}} + 2h_{\text{s}} + 2h_{\text{bi}} \tag{3.37}$$

3.4 Rotor geometry

As already said in section [2.4], the rotor winding is absent and the electromagnetic torque generation is due to the rotor topology. Therefore, the rotor design requires a particular attention from a mechanical point of view. Indeed a not perfect rotor geometry leads to unacceptable motor electromagnetic performances. The parameters influencing the motor performances are individually investigated in order to identify the trade-offs between the electromagnetic and mechanical performances of the motor (see fig.[3.1]).

Selecting the airgap value g, the rotor diameter D_{r} is obtained from the inner stator diameter $D_{\text{s,i}}$. The shaft diameter D_{shf} is chosen avoiding the resonance frequencies [25]:

$$D_{\text{shf}} = (0.20 - 0.25)D_{\text{r}} \tag{3.38}$$

3.4.1 Flux barriers per pole N_{b}

Under load conditions the completely saturated rotor iron ribs could be considered magnetically as equivalent rotor slots. Therefore, let Q_{r} the equivalent rotor slots number and $n_{\text{r}} = \frac{Q_{\text{r}}}{2p}$ the equivalent rotor slots per pole number equally distributed on the rotor circumference.

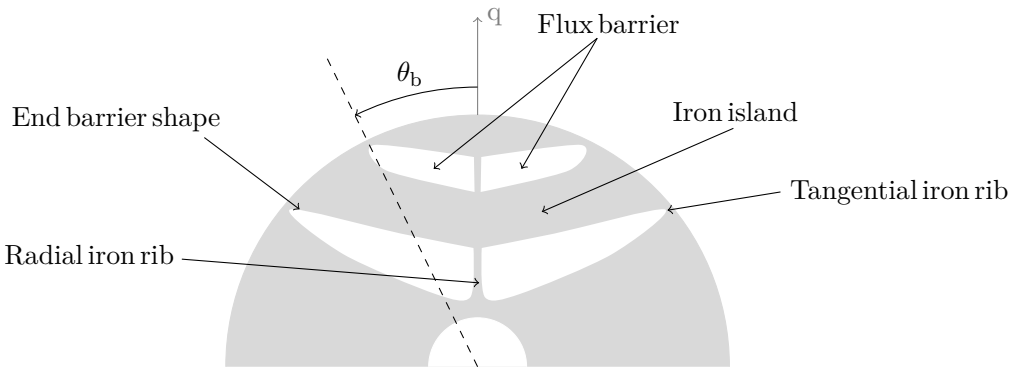

Figure 3.1 – Two flux barriers per pole rotor sketch

While the rotor is moving, the stator scalar magnetic potential U_s sees along the airgap a succession of iron islands and iron ribs as if it was a succession of rotor teeth and rotor slots. The interaction between the stator scalar magnetic potential U_s and this succession of different permanence magnetic paths generates high order spatial harmonics that could be attenuated adopting a number of equivalent rotor slots Q_r equal to or multiple of Q_s.

A suggested n_r value is obtained considering that the higher number of iron islands per pole, the lower are the rotor iron losses [9]. Due to mechanical and manufacturing reasons the number of iron islands per pole must be limited and consequently the number of flux barriers per pole N_b:

$$n_r = \frac{Q_s}{2p} \pm 2 \tag{3.39}$$

$$2 \leq N_b \leq 4 \tag{3.40}$$

3.4.2 End flux barriers angles θ_b

The number of equivalent rotor slots Q_r represents the actual or fictitious flux barriers end points and they play a fundamental role in determining the torque ripple.

Taken as reference the q-axis and therefore considering an half pole, the flux barrier end points define the flux barrier end angles θ_b. These angles are equally distributed along the rotor circumference, although this assumption does not guarantee the lowest torque ripple solution (see fig.[3.2]).

As first design assumption, the flux barrier end angles θ_b are spaced by the electrical equivalent rotor slot pitch angle α_r^e:

$$\alpha_r^e = p\,\frac{2\pi}{Q_r} \tag{3.41}$$

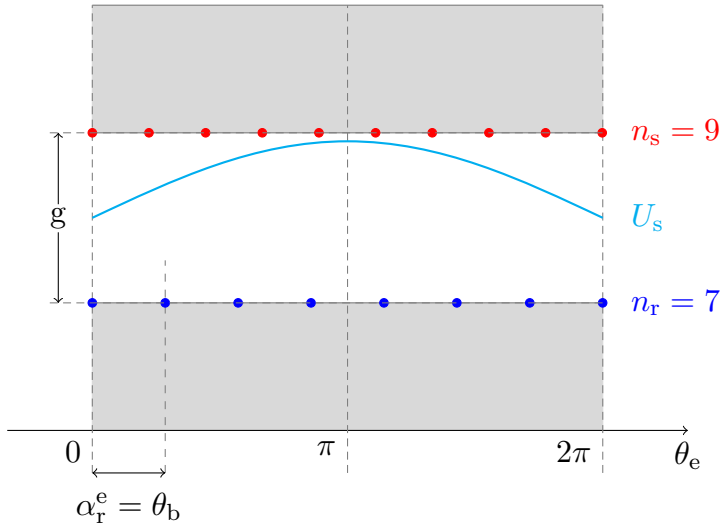

Figure 3.2 – End flux barrier angles θ_b

3.4.3 Rotor insulation coefficient K_{air}^r

As said before in chapter [3], one of the rotor design principle consists of minimizing the q-axis flux component keeping the total flux barriers thickness τ_b as large as possible. The increase of the total flux barriers thickness τ_b leads to an high saturation level in some stator teeth and consequently to a flux density reduction. This condition not involves any benefit regarding high average torque value achievement because the d-axis flux component is obstructed by the stator teeth saturation. Therefore, it is convenient to find a compromise between the rotor saturation level and the d-axis flux component maximizing capability. A perfect balance between the total flux barriers thickness τ_b and the total iron islands thickness τ_i has to be reached to maximize the motor electromagnetic performances.

To evaluate this issue, the rotor insulation coefficient along the q-axis K_{air}^r is defined as following:

$$K_{air}^r = \frac{\tau_b}{\frac{D_r - D_{shf}}{2}} \tag{3.42}$$

In order to saturate equally the machine achieving an high torque value and to decrease the stator losses, the rotor insulation coefficient along the q-axis K_{air}^r has to be selected slightly higher than the stator saturation coefficient K_{sat}^s [14]:

$$K_{sat}^s = \frac{p_s - w_t}{p_s} \tag{3.43}$$

The total flux barriers thickness τ_b and the total iron islands thickness τ_i are obtained from equation (3.42) and from the following dimensional constrain:

$$\tau_b + \tau_i = \frac{D_r - D_{shf}}{2} \tag{3.44}$$

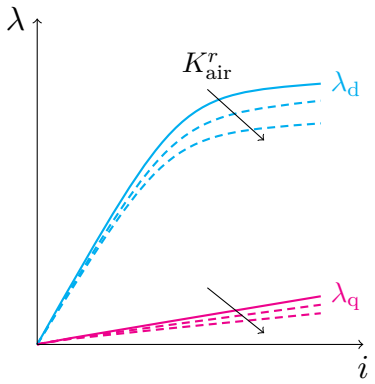

Figure 3.3 – Rotor insulation coefficient K^r_{air} variation effect on dq-flux linkage components

In fig.[3.3] the effect of the rotor insulation coefficient $K^{\text{r}}_{\text{air}}$ variation on the d-axis flux linkage component λ_{d} and on the q-axis flux linkage component λ_{q} is qualitatively shown. In particular increasing the rotor insulation coefficient $K^{\text{r}}_{\text{air}}$ the d-axis flux linkage component λ_{d} decrease is greater than the q-axis flux linkage component λ_{q} decrease. This result is due to the greater presence of iron magnetic paths along the d-axis than along the q-axis that are more affected by saturation effect.

3.4.4 Flux barriers profile and thickness t_{b}

The main principle of the rotor design consists of maximizing the d-axis flux component guiding the magnetic field flux lines along the minimum magnetic reluctance paths. A suggested method presented is to consider the natural flow patters of the magnetic field potential lines in a solid rotor in order to define the iron islands and flux barriers profiles [9] [16]. The rotor scalar magnetic potential U_{r} represents the potential of the magnetic field lines and then it identifies the maximum permeance magnetic paths in the rotor. From Maxwell's equations the rotor scalar magnetic potential U_{r} expression could not be obtained in an analytical way.

The expression of the magnetic field potential lines in a solid rotor could be approximated from the conformal mapping theory and the Joukowski airfoil potential formulation (see fig.[3.4]). Considering a circular sector domain described in the polar coordinates (ρ,θ):

$$r_{\text{shf}} \leq \rho \leq r_{\text{r}} \tag{3.45}$$

$$0 \leq \theta \leq \frac{\pi}{p} \tag{3.46}$$

the magnetic field potential line is expressed as:

$$U = \frac{\left(\frac{\rho}{r_{\text{shf}}}\right)^{2p} - 1}{\left(\frac{\rho}{r_{\text{shf}}}\right)^{p}} \cdot \sin(p\theta) \tag{3.47}$$

where r_{r} and r_{shf} are the rotor and shaft radius respectively. The magnetic potential U_{b} related to the flux barrier is calculated at the ρ coordinate equal to the rotor diameter r_{r} and at the θ coordinate related to the end flux barrier angle θ_{b}.

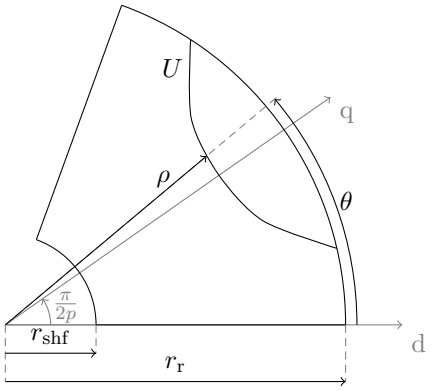

Figure 3.4 – Magnetic potential lines in a solid rotor based on [16]

The mean radius r_b of the flux barrier is calculated on the q-axis angular position from its magnetic potential U_b:

$$U_\mathrm{b} = \frac{\left(\frac{r_\mathrm{r}}{r_\mathrm{shf}}\right)^{2p} - 1}{\left(\frac{r_\mathrm{r}}{r_\mathrm{shf}}\right)^{p}} \cdot \sin(p\theta_\mathrm{b} + \frac{\pi}{2}) \tag{3.48}$$

$$r_\mathrm{b} = r_\mathrm{shf} \cdot \sqrt[p]{\frac{U_\mathrm{b} + \sqrt{U_\mathrm{b}^2 + 4\sin^2(\frac{\pi}{2})}}{2\sin(\frac{\pi}{2})}} \tag{3.49}$$

The flux barrier thickness t_b is computed considering the iron islands as shown in fig.[3.5].

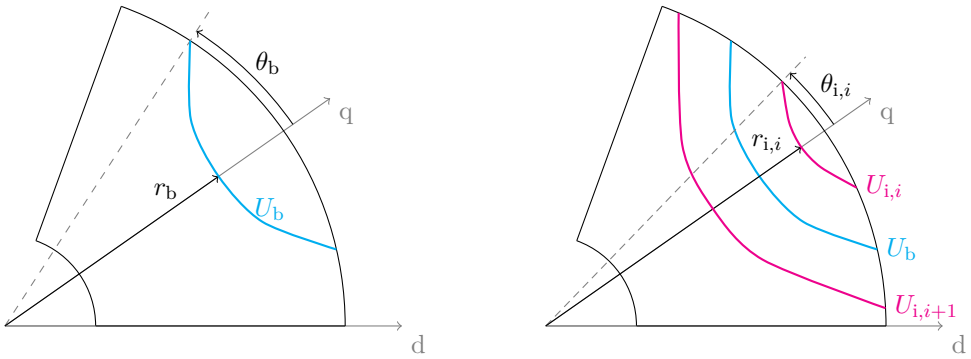

Figure 3.5 – Flux barrier and iron island mean profile

According to the same drawing procedure to calculate the mean radius of the flux barrier r_b, the mean radius of the iron island r_i is obtained considering the end iron island angle θ_i. The end iron island angle θ_i is defined as:

$$\theta_\mathrm{i} = \frac{\theta_{\mathrm{b},i}^{\mathrm{m}} - \theta_{\mathrm{b},i-1}{}^{\mathrm{m}}}{2} \tag{3.50}$$

where $i = 0, 1, 2, ..., N_\mathrm{b}$. Therefore, the iron island potential U_i and mean radius r_i are:

$$U_\mathrm{i} = \frac{\left(\frac{r_\mathrm{r}}{r_\mathrm{shf}}\right)^{2p} - 1}{\left(\frac{r_\mathrm{r}}{r_\mathrm{shf}}\right)^{p}} \cdot \sin(p\theta_\mathrm{i} + \frac{\pi}{2}) \tag{3.51}$$

$$r_\mathrm{i} = r_\mathrm{shf} \cdot \sqrt[p]{\frac{U_\mathrm{i} + \sqrt{U_\mathrm{i}^2 + 4\sin^2(\frac{\pi}{2})}}{2\sin(\frac{\pi}{2})}} \tag{3.52}$$

The maximum allowed flux barrier thickness t_b along the q-axis is computed considering the rotor saturation coefficient along the q-axis $K_\mathrm{air}^\mathrm{r}$:

$$t_\mathrm{b} = 2\ K_\mathrm{air}^\mathrm{r} \cdot \min(r_{\mathrm{i},1} - r_\mathrm{b}; r_\mathrm{b} - r_{\mathrm{i},i+1}) \tag{3.53}$$

According to the flux barrier thickness t_b, the upper $r_\mathrm{b,up}$ and lower $r_\mathrm{b,low}$ flux barrier radius are obtained. The flux barrier profile could be drawn following the magnetic field potential lines corresponding to the upper and lower flux barrier radii (see fig.[3.6]).

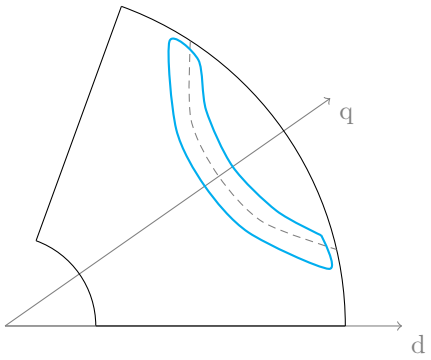

Figure 3.6 – Flux barrier profile

3.4.5 Iron ribs thickness t_rib

To achieve a mechanically self-sustained rotor it is necessary to introduce tangential ribs along the airgap $t_\mathrm{rib}^\mathrm{t}$ and radial ribs along the q-axis $t_\mathrm{rib}^\mathrm{r}$. During load conditions these ribs are completely saturated by the d-axis stator scalar magnetic potential U_s^d and the magnetic flux necessary to saturate them causes a torque reduction. From a magnetic point of view, the iron ribs represent a magnetic short circuit reducing the flux per pole Φ and therefore their introduction leads to a magnetizing saliency ratio ξ_m decrease. For example in synchronous reluctance machines for traction drive applications, the iron ribs design requires particular care due to high reliability demand during the service life and due to a severe traction profile characterized by frequent accelerations and regenerative braking. Considering the steady-state mechanical angular speed ω_m and neglecting the effects of the temperature, vibrations and shaft dynamical forces; the structural rotor integrity against static failure and fatigue failure is investigated [4].

Static stress analysis

The static resistance is evaluated by the classic mechanical structural design based on the stress averaged over the reduced section. The i-th iron rib thickness $t_{\mathrm{rib},i} = t^{\mathrm{t}}_{\mathrm{rib},i} + t^{\mathrm{r}}_{\mathrm{rib},i}$ has to sustain the magnetic and centrifugal force acting on the i-th iron island (see fig.[3.7]). In particular the magnetic force F_{m} is the magnetic pressure $\frac{\hat{B}_g}{2\mu_0}$ that the airgap flux density B_g applies to the rotor surface $\theta_b\, D_{\mathrm{r}}\, L_{\mathrm{stk}}$. The centrifugal force $F_{\mathrm{c}} = m\, R_{\mathrm{c}}\, \omega^2_{\mathrm{m}}$ is the force acting on the center of gravity of the i-th iron island due to the rotor mechanical speed ω_{m}.

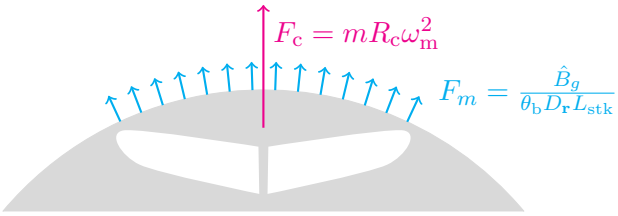

Figure 3.7 – Forces acting on the i-th iron island

Assuming a circular flux barrier according to the magnetic potential lines and a rotor mechanical overspeed $\omega_{\mathrm{os}} = 1.25\,\omega_{\mathrm{m}}$, the resulting force F_{r} acting on the i-th iron island is:

$$F_{\mathrm{r}} = \theta_{\mathrm{b},i} D_{\mathbf{r}} L_{\mathrm{stk}} \left[\frac{\hat{B}^2_{\mathrm{g}}}{2\mu_0} + \frac{\gamma_{\mathrm{iron}} D^2_{\mathrm{r}} \omega^2_{\mathrm{os}} \cdot \cos(\theta_{\mathrm{b},i})}{4} \left(1 - \frac{\sin(2\theta_{\mathrm{b},i})}{2\theta_{\mathrm{b},i}} \right) \right] \tag{3.54}$$

Therefore, the i-th iron rib thickness $t_{\mathrm{rib},i}$ is:

$$t_{\mathrm{rib},i} = K_{\mathrm{sf}} \cdot \frac{F_{\mathrm{r}}}{\sigma_{\mathrm{s}} L_{\mathrm{stk}}} \tag{3.55}$$

where σ_{s} $\frac{\mathrm{N}}{\mathrm{m}^2}$ is the lamination tensile strength and K_{sf} is a safety factor. As starting design assumption, the safety factor K_{sf} is selected equal to 2.7 in a precautionary way. The tangential ribs thickness $t^{\mathrm{t}}_{\mathrm{rib}}$ has to be limited to not decrease the electromagnetic performances of the motor. On the other hand, the minimum tangential ribs thickness $t^{\mathrm{t}}_{\mathrm{rib}}$ has to be equal to the lamination one due to manufacturing constrains. Therefore, the i-th iron rib thickness $t_{\mathrm{rib},i}$ has to be distributed between the tangential ribs thickness $t^{\mathrm{t}}_{\mathrm{rib},i}$ and the radial ribs thickness $t^{\mathrm{r}}_{\mathrm{rib},i}$.

Fatigue stress analysis

The radial iron ribs $t^{\mathrm{r}}_{\mathrm{rib}}$ have to be designed accurately due to their mechanical support function. In order to increase the radial iron ribs $t^{\mathrm{r}}_{\mathrm{rib}}$ saturation to not degrade the magnetizing saliency ratio ξ_{m}, sharp corners for the flux barriers are generally adopted. This geometrical solution leads to an high mechanical stress in the end flux barrier region along the q-axis.

The design approach based on material data sheet underestimates the service life of this geometric solution because its fatigue behavior is similar to that of a sharp V-notch and it leads to a stress singularity which does not allow to use the classic approach to fatigue analysis. As starting design assumption, the i-th iron rib thickness $t_{\mathrm{rib},i}$ estimated in equation

(3.55) is adopted only to design the the radial ribs thickness $t^{\mathrm{r}}_{\mathrm{rib},i}$; whereas the tangential ribs thickness $t^{\mathrm{t}}_{\mathrm{rib}}$ is assumed equal to the lamination one.

3.4.6 End flux barriers shape configurations

As already explained, the flux barriers profile plays a significant role on average torque maximization and torque ripple reduction. In particular not only the flux barriers angular position at the airgap θ_{b} but also the end flux barriers shape influence the electromagnetic and mostly structural performances of the machine. It is therefore necessary to identify the trade-offs between the electromagnetic and structural performances of the machine in order to guarantee a mechanically self-sustained rotor. Sharp end flux barriers and the round end flux barriers configurations could be adopted to achieve specific electromagnetic and structural machine performances (see fig.[3.8]).

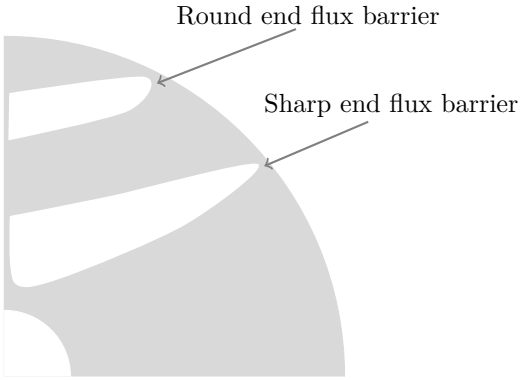

Figure 3.8 – End flux barrier shapes

Sharp end flux barriers configuration

The sharp end flux barrier is made by one tangential straight segment along the airgap connected to the flux barrier profile lines. The tangential straight segment length variation influences flux density distribution and the local von Mises mechanical stress distribution in the end flux barriers region. Therefore, it is possible to implement optimizing algorithms that modify the tangential straight segment length in order to obtain specific performances.

Considering the flux density distribution in the end flux barriers region, as the tangential straight segment length increases, the tangential iron rib $t^{\mathrm{t}}_{\mathrm{rib}}$ changes its angular position and tends to be splitted in two different saturated iron regions. The number of equivalent rotor slot Q_{r} increases and consequently the interaction between the number of stator slot Q_{s} and the not optimal equivalent rotor slots distribution leads to a torque ripple increase as explained in section [3.4.1].

As said before the local von Mises mechanical stress distribution in the end flux barriers region is related to the tangential straight segment length. In particular as the tangential

straight segment length increases, the maximum mechanical stress decreases. Indeed as the tangential straight segment length increases, the von Mises mechanical stress distribution in the end flux barriers region becomes more uniformly distributed and consequently the maximum mechanical stress decreases.

Round end flux barriers configuration

The round end flux barrier is made by two arcs joining together in a point near the airgap. This geometrical configuration derived from the sharp end flux barrier configuration assuming a null tangential straight segment length.

Electromagnetic and structural comparison

The sharp end flux barriers and the round end flux barriers configurations are compared in electromagnetic and structural performances terms in order to individuate the optimal design starting assumption [10]:

- The average torque value is quite constant for all the end flux barriers configurations;
- Sharp end flux barriers present the lowest torque ripple value but the highest mechanical stress in the end flux barriers region;
- Round end flux barriers present the highest torque ripple value but the lowest mechanical stress in the end flux barriers region.

Depending on the specific design aims, the proper end flux barriers configuration could be adopted. In order to minimize the torque ripple, the sharp end flux barriers configuration is selected during the design process in chapter [4]. In particular the end flux barrier are drawn as a tangential straight segment along the airgap connected to the flux barrier profile lines. Due to the high mechanical stress in the end flux barriers region, the tangential ribs thickness $t_{\mathrm{rib}}^{\mathrm{t}}$ is assumed twice the lamination one.

4 Synchronous Reluctance Motor Design

The initial data of a three-phase squirrel cage induction motor are considered to start the synchronous reluctance motor design [21]. The induction motor at issue is designed for industrial applications and then the resultant synchronous reluctance motor design can not be compared to electric motors for automotive purposes. Nevertheless, the design concept general validity allows to apply the design process to every application requirements.

The motor specifications are:

- Nominal power $P_\mathrm{n} = 30\,\mathrm{kW}$
- Synchronous speed $n_\mathrm{n} = 1500\,\mathrm{rpm}$
- Number of phases $m = 3$
- Nominal line-to-line voltage $V_\mathrm{n} = 690\,\mathrm{V}$
- Efficiency $\eta = 92\%$

4.1 Main motor dimensions

According to chapter [3], main motor parameters are deduced selecting the number of pole pairs p, the number of slots per pole and per phase q and the airgap thickness g:

- Pole pairs $p = 2$
- Number of slots per pole and per phase $q = 3$
- Airgap thickness $\mathrm{g} = 0.35\,\mathrm{mm}$
- Nominal frequency $f_\mathrm{n} = 50\,\mathrm{Hz}$
- Nominal mechanical and electrical speed $\omega_\mathrm{m}^\mathrm{e} = p\,\omega_\mathrm{m} = 100\pi\,\frac{\mathrm{rad}}{\mathrm{s}}$
- Nominal torque $T_\mathrm{n} = 190\,\mathrm{Nm}$
- Number of stator slots $Q_\mathrm{s} = 36$
- Electrical slot angle $\alpha_\mathrm{s}^\mathrm{e} = 20°$
- Electrical chording angle $\beta_\mathrm{s}^\mathrm{e} = 20°$
- Fundamental winding coefficient $(K_\mathrm{w})_1 = K_\mathrm{w} = 0.95$

The equivalent magnetic airgap along the d-axis g_d is the most critical assumption regarding the first design step. The Carter coefficient K_c and the saturation coefficient along the d-axis K_{sat}^d are difficult to estimate in advance [6]. As starting design assumptions, the rotor Carter coefficient K_c^r is hypothesized equal to the stator Carter coefficient K_c^s as if the saturated iron ribs were geometrically equal to the stator slots Q_s. Furthermore, the saturation coefficient along the d-axis K_{sat}^d is assumed according equation (3.15):

$$K_c^s = K_c^r = 1.15 \tag{4.1}$$

$$K_{sat}^d = 1.4 \tag{4.2}$$

$$g_d = g\, K_c^s\, K_c^r\, K_{sat}^d = 0.65\,\text{mm} \tag{4.3}$$

The design process focuses on maximizing torque density and therefore the magnetizing current I_d is limited by assuming the angle α_i^e greater than 45°:

$$\alpha_i^e = 65^\circ \tag{4.4}$$

Assuming a d-axis airgap flux density component $\hat{B}_g^d = 1\,\text{T}$, the stator scalar magnetic potential components are obtained as:

$$\hat{U}_s^d = \frac{g_d\, \hat{B}_g^d}{\mu_0} = 517\,\text{A} \tag{4.5}$$

$$\hat{U}_s^q = \hat{U}_s^d \cdot \tan(\alpha_i^e) = 1108\,\text{A} \tag{4.6}$$

$$\hat{U}_s = 1222\,\text{A} \tag{4.7}$$

The fictitious rotor flux density $\hat{B}_r$ is consequently:

$$\hat{B}_r = \mu_0 \frac{\hat{U}_s}{2g_d} = 1.18\,\text{T} \tag{4.8}$$

Finally the main machine geometry are estimated:

$$L_{stk}\, D_{s,i} = \frac{2\, T_n}{\pi\, \hat{B}_r\, p\, \hat{U}_s \cdot \sin(2\alpha_i^e)} = 0.055\,\text{m}^2 \tag{4.9}$$

As starting design assumption the inner stator diameter $D_{s,i}$ and the stack length L_{stk} are assumed equal to achieve a compact machine:

$$L_{stk} = D_{s,i} = 0.235\,\text{m} \tag{4.10}$$

4.2 Electrical parameters

According to section [3.2.1], a fast evaluation of the main motor electrical parameters is obtained. Assuming an inner voltage drop of 0.5%, and fixing the machine efficiency $\eta = 95\%$ and the power factor $\varphi = 0.80$; the winding voltage V_w and the nominal current I_n are estimated:

$$V_w = 0.95 \frac{V_n}{\sqrt{3}} = 378\,\text{V} \tag{4.11}$$

$$I_n = \frac{P_n}{3\, V_w\, \eta \cdot \cos(\varphi)} = 33\,\text{A} \tag{4.12}$$

Having adopted an AC double layer distributed winding the number of equivalent series conductors per slot n_{cs} has to be integer and even:

$$n_{\mathrm{cs}} = \frac{\pi \hat{U}_{\mathrm{s}}^{\mathrm{d}}}{3K_{\mathrm{w}}\, q\, \hat{I}_{\mathrm{d}}} = 12 \tag{4.13}$$

According to the parallel paths $n_{\mathrm{pp}} = 2$, the actual number of conductors per phase N and per slot n_{c}, are:

$$N_{\mathrm{c}} = n_{\mathrm{pp}}\, N_{\mathrm{s}} = 288 \tag{4.14}$$

$$n_{\mathrm{c}} = n_{\mathrm{pp}}\, n_{\mathrm{cs}} = 24 \tag{4.15}$$

where $N_{\mathrm{s}} = 144$ is the number of equivalent series conductors per phase. Finally it is possible to estimate the fundamental flux per pole $\hat{\Phi}$:

$$\hat{\Phi} = \frac{\sqrt{2}\, V_{\mathrm{w}}}{\pi\, K_{\mathrm{w}}\, f_{\mathrm{n}}\, N_{\mathrm{s}}} = 0.276\,\mathrm{Wb} \tag{4.16}$$

and the fundamental linkage flux $\hat{\Lambda}$ of a phase:

$$\hat{\Lambda} = \frac{K_{\mathrm{w}}\, N_{\mathrm{s}}}{p}\hat{\Phi} = 1.88\,\mathrm{Vs} \tag{4.17}$$

4.3 Stator and rotor parameters

In sections [3.3] and [3.4] are presented a rough stator geometry estimation and a deeply discussion about the rotor topology. From a magnetic point of view the wedge height h_{wdg}, the slot opening width w_{so} and height h_{so} are designed as small as possible ensuring anyway the stator winding mechanical introduction [6]. The main stator and rotor parameters are resumed in tab.[4.1].

Table 4.1 – Stator and rotor geometrical parameters

Stator parameter	**Rotor parameter**
$D_{\mathrm{s,e}} = 320\,\mathrm{mm}$	$D_{\mathrm{r}} = 234.3\,\mathrm{mm}$
$D_{\mathrm{s,i}} = 235\,\mathrm{mm}$	$D_{\mathrm{shf}} = 52.7\,\mathrm{mm}$
$h_{\mathrm{s}} = 16\,\mathrm{mm}$	$\theta_{\mathrm{b,1}} = 13°$
$w_{\mathrm{t}} = 13\,\mathrm{mm}$	$\theta_{\mathrm{b,2}} = 26°$
$w_{\mathrm{s,i}} = 7.5\,\mathrm{mm}$	$\theta_{\mathrm{b,3}} = 39°$
$w_{\mathrm{s,i}} = 8\,\mathrm{mm}$	$K_{\mathrm{air}}^{\mathrm{r}} = 0.52$
$w_{\mathrm{so}} = 2\,\mathrm{mm}$	$t_{\mathrm{rib}}^{\mathrm{t}} = 0.7\,\mathrm{mm}$
$h_{\mathrm{so}} = 2.5\,\mathrm{mm}$	$t_{\mathrm{rib,2}}^{\mathrm{r}} = 1.2\,\mathrm{mm}$
$h_{\mathrm{wdg}} = 2\,\mathrm{mm}$	$t_{\mathrm{rib,3}}^{\mathrm{r}} = 1.4\,\mathrm{mm}$

5 Rotor Geometry Analysis

The parameters influencing the motor performances are modified properly in order to achieve the required performances:

- Rotor insulation coefficient $K^{\mathrm{r}}_{\mathrm{air}}$
- End flux barrier angles θ_{b}

These parameters are individually investigated assuming valid the superposition principle and neglecting the high saturation operating conditions of synchronous reluctance machines. The following rotor geometry analysis process is effectuated by the finite elements software Flux2D by Altair and leads to an improvement of motor performances modifying properly its topology. The selected rotor solutions aim to maximize the average torque value T_{avg} and to decrease as much as possible the torque ripple value Δ_T.

5.1 Motor sizing for high torque density

Sizing in high torque density terms means to individuate the minimum motor dimensions that guarantee the nominal torque value T_{n} for fixed nominal power P_{n} and geometry. Assume $\epsilon = \frac{D_{\mathrm{s,e}}}{D_{\mathrm{s,i}}}$ the ratio between the external stator diameter $D_{\mathrm{s,e}}$ and the inner stator diameter $D_{\mathrm{s,i}}$. The motor torque density δ_{t} is evaluated in function of the rotor diameter D_{r}, the ratio ϵ and the motor stack length L_{stk}. For fixed airgap g value, the inner stator diameter $D_{\mathrm{s,i}}$ value is varied being directly related to the rotor diameter D_{r}.

In particular the motor torque density δ_{t}, the average torque value T_{avg} and the torque ripple Δ_T are investigated for:

- $205\,\mathrm{mm} \leq D_{\mathrm{s,i}} \leq 235\,\mathrm{mm}$
- $1.4 \leq \epsilon \leq 1.5$
- $205\,\mathrm{mm} \leq L_{\mathrm{stk}} \leq 235\,\mathrm{mm}$

Due to manufacturing constrains, only the motors dimensions suitable in constructional and assembly terms are simulated. Furthermore, only the motors dimensions ensuring an average torque value T_{avg} around the nominal one T_{n} are considered.

Simulations results show that the average torque value T_{avg} is proportional to the rotor diameter D_{r} and to the motor stack length L_{stk} as already expressed by equation (2.77). The external stator diameter $D_{s,e}$ influences the average torque value T_{avg} because a low value of the parameter ϵ leads to a saturated stator and consequently to an average torque value T_{avg} decrease. The torque ripple Δ_T value is not affected by the rotor diameter D_{r} and by the motor stack length L_{stk}, while it is inversely proportional to the ϵ parameter value.

The motor dimensions adopted to proceed with the analysis process are presented in tab.[5.1]. Among the simulations these motor dimensions lead to an average torque value $T_{\text{avg}} = 188.80\,\text{Nm}$, a torque ripple value $\Delta_T = 13\%$ and guarantee the highest torque density value $\delta_{\text{t}} = 10.08\,\frac{\text{kNm}}{\text{m}^3}$. Generally the synchronous reluctance motors exhibit a torque density value δ_t between $7 - 12\,\frac{\text{kNm}}{\text{m}^3}$ depending on the cooling system effectiveness and on the motor size. Therefore, the torque density value $\delta_{\text{t}} = 10.08\,\frac{\text{kNm}}{\text{m}^3}$ achieved is reasonable taking into account the standard cooling system adopted and the not small motor size [9].

Table 5.1 – Motor main dimensions

$D_{\text{s,e}}$	$= 318\,\text{mm}$
$D_{\text{s,i}}$	$= 212.5\,\text{mm}$
D_{r}	$= 211.8\,\text{mm}$
D_{shf}	$= 47.65\,\text{mm}$
L_{stk}	$= 235\,\text{mm}$
δ_{t}	$= 10.08\,\frac{\text{kNm}}{\text{m}^3}$

5.2 Rotor insulation coefficient $K^{\text{r}}_{\text{air}}$ analysis

The rotor insulation coefficient $K^{\text{r}}_{\text{air}}$ defines the total flux barriers thickness τ_{b} introduced in the rotor along the q-axis. Rotor saturation coefficient $K^{\text{r}}_{\text{air}}$ variations influence the electromagnetic torque average value and ripple. As starting design assumption it has be selected considering the stator saturation coefficient $K^{\text{s}}_{\text{sat}}$ in order to saturate equally the motor.

The electromagnetic torque profile is investigated in function of the rotor insulation coefficient $K^{\text{r}}_{\text{air}}$ from 0.35 to 0.55.

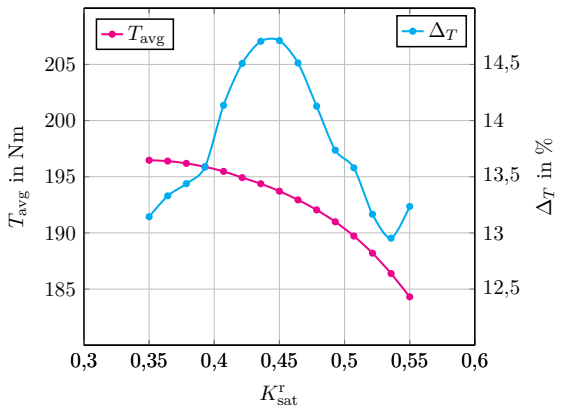

Figure 5.1 – Torque profile in function of the rotor insulation coefficient $K^{\text{r}}_{\text{air}}$

According to fig.[5.1] a lower rotor insulation coefficient $K^{\mathrm{r}}_{\mathrm{air}}$ value leads to an higher average torque value T_{avg} helping the d-axis flux circulation. In particular the starting design assumption $K^{\mathrm{r}}_{\mathrm{air}} = 0.52$ guarantees the lowest torque ripple value Δ_T at the expense of the average torque value T_{avg}. The rotor insulation coefficient $K^{\mathrm{r}}_{\mathrm{sat}} = 0.35$ is adopted to proceed with the analysis process ensuring the highest average torque value T_{avg} and also a low torque ripple value Δ_T among the simulations.

5.3 End flux barrier angles θ_{b} analysis

The starting design assumption consists in equally distributed end flux barriers angles θ_{b} along the rotor circumference. Furthermore, the first end flux barrier angle $\theta_{\mathrm{b},1}$ has been assumed equal to the electrical equivalent rotor slot pitch angle $\alpha^{\mathrm{e}}_{\mathrm{r}}$, as explained in section [3.4.2]. Generally this starting design assumption does not guarantee the lowest torque ripple solution. The end flux barriers angles θ_{b} are shifted from their symmetrical position in order to find a more advantageous combination between the number of stator slots Q_{s} and the number of equivalent rotor slots Q_{r} in torque ripple terms.

A suggested method is presented to estimate the suitable end flux barriers angles θ_{b} positions in torque ripple Δ_T terms [3]. This method is limited to only one or two flux barriers per pole and then for a more complex rotor geometry this approach can not be applied.

The torque ripple value Δ_T is investigated for the following end flux barriers angles θ_{b} combinations:

- $13° \leq \theta_{\mathrm{b},1} \leq 15°$
- $26° \leq \theta_{\mathrm{b},2} \leq 27°$
- $39° \leq \theta_{\mathrm{b},3} \leq 40°$

Only the end flux barriers angles θ_{b} combinations leading to low torque ripple values Δ_T are showed in fig.[5.2]. In particular the torque ripple Δ_T profile is plotted in function of the end flux barrier angle $\theta_{\mathrm{b},1}$ for a fixed $\theta_{\mathrm{b},2}$ and $\theta_{\mathrm{b},3}$ combination.

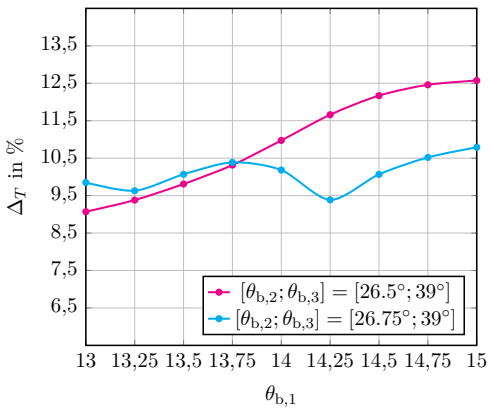

Figure 5.2 – Torque ripple value Δ_T in function of the end flux barriers angle $\theta_{b,1}$ for a fixed $\theta_{b,2}$ and $\theta_{b,3}$ combination

The end flux barriers angles $[\theta_{b,1}; \theta_{b,2}; \theta_{b,3}] = [13°; 26.5°; 39°]$ combination ensures the lowest torque ripple value $\Delta_T = 9.07\%$ and it is adopted to proceed with the analysis process. It is worthy to note that the adopted solution is very close to the assumed combinations certifying the rotor design validity shown in section [3.4.2]. Furthermore, a 2% second end barrier angle $\theta_{b,2}$ increment leads approximately to a 30% torque ripple value Δ_T relative decrease confirming the delicate relation between the rotor topology and the motor performances.

5.4 Max Torque per Ampere (MTPA) condition

For a fixed geometry and a fixed current value I, the max torque per ampere condition is individuated varying the electrical current angle α_i^e in the (d,q) system of reference. For the current values $I = \frac{2}{3}I_n, I_n$ and $\frac{3}{2}I_n$ the average torque value T_{avg} is investigated in order to individuate the electrical current angle ensuring the MTPA condition α^e_{MTPA}.

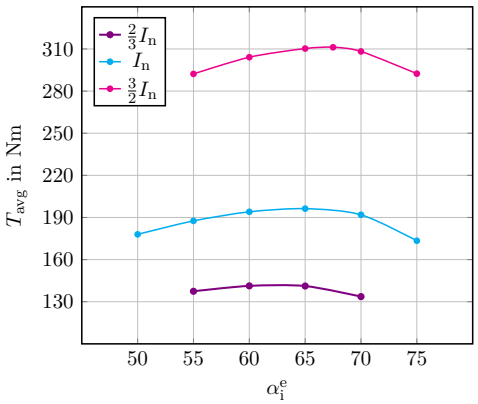

Figure 5.3 – MTPA condition in function of the electrical current angle α_i^e

In fig.[5.3] the average torque value T_{avg} is calculated for each current values I and for the electrical current angle α_i^e from 50° to 75°. For the nominal current value I_n the MTPA electrical current angle α^e_{MTPA} is equal to 65° accordingly to the starting design assumption. Furthermore, for the current value $\frac{3}{2}I_n$ the MTPA electrical current angle α^e_{MTPA} shifts to a greater electrical current angle α_i^e due to to the saturation effect caused by the higher current value. On the contrary, for the current value $\frac{2}{3}I_n$ the MTPA electrical current angle α^e_{MTPA} shifts to a lower electrical current angle α_i^e thanks to the low motor saturation level.

It is also interesting to express the torque ripple value Δ_T in function of the current value I and of the electrical current angle α_i^e. For the nominal current value I_n the lowest torque ripple values Δ_T are individuated around the MTPA electrical current angle α^e_{MTPA} and in particular at the electrical current angle $\alpha_i^e = 60°$, as shown in fig.[5.4]. Also the torque ripple value Δ_T profile depends on the current value I. In overload condition the torque ripple value Δ_T increases and it is quite constant for a wide electrical current angles α_i^e range. For the current value $\frac{2}{3}I_n$ the torque ripple value Δ_T increases quickly after having reached it minimum value. At the MTPA electrical current angle α^e_{MTPA} the lowest torque ripple value Δ_T is obtained for the nominal condition.

The electrical current angle $\alpha_{\mathrm{i}}^{\mathrm{e}} = 65°$ is adopted to to proceed with the analysis process because it guarantees the max torque per ampere condition and a low torque ripple value at the nominal operating condition.

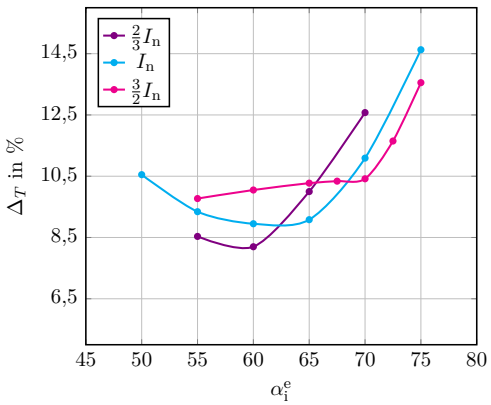

Figure 5.4 – Torque ripple value Δ_T in function of the electrical current angle $\alpha_{\mathrm{i}}^{\mathrm{e}}$

5.5 Motor geometry

Having adopted the solutions presented in chapter [5], the motor dimensions are re-sized in order to achieve the nominal torque value T_{n} (see fig.[5.5]). According to the results shown in section [5.1], the stack length L_{stk} is decreased, being proportional to the electromagnetic torque generated at the shaft. The resulting motor dimensions and electrical parameters are resumed in tab.[5.2].

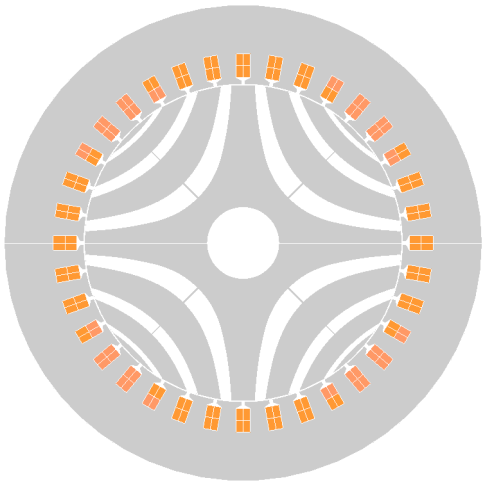

Figure 5.5 – Motor cross section

Table 5.2 – Motor geometrical and electrical parameters

Motor dimension	Rotor parameter	Electrical parameter
$D_{\mathrm{s,e}} = 318\,\mathrm{mm}$	$\theta_{\mathrm{b},1} = 13°$	$\eta = 0.95$
$D_{\mathrm{s,i}} = 212.5\,\mathrm{mm}$	$\theta_{\mathrm{b},2} = 26.5°$	$I_{\mathrm{n}} = 33\,\mathrm{A}$
$D_{\mathrm{r}} = 211.8\,\mathrm{mm}$	$\theta_{\mathrm{b},3} = 39°$	$N_{\mathrm{c}} = 288$
$D_{\mathrm{shf}} = 47.65\,\mathrm{mm}$	$K^{\mathrm{r}}_{\mathrm{air}} = 0.35$	$N_{\mathrm{s}} = 144$
$L_{\mathrm{stk}} = 227.5\,\mathrm{mm}$	$t^{\mathrm{t}}_{\mathrm{rib}} = 0.7\,\mathrm{mm}$	$n_{\mathrm{cs}} = 12$
$\epsilon = 1.5$	$t^{\mathrm{r}}_{\mathrm{rib},2} = 1.3\,\mathrm{mm}$	$J_{\mathrm{s}} = 8.3\,\frac{\mathrm{A}}{\mathrm{mm}^2}$
$\delta_{\mathrm{t}} = 10.5\,\frac{\mathrm{kNm}}{\mathrm{m}^3}$	$t^{\mathrm{r}}_{\mathrm{rib},3} = 1.4\,\mathrm{mm}$	$\alpha^{\mathrm{e}}_{\mathrm{i}} = 65°$

The designed synchronous reluctance motor results to be competitive in volumetric torque density δ_{t} terms compared to the starting induction motor (see tab.[5.3]).

Table 5.3 – Induction motor main dimensions

$D_{\mathrm{s,e}} = 335\,\mathrm{mm}$
$D_{\mathrm{r}} = 200\,\mathrm{mm}$
$L_{\mathrm{stk}} = 200\,\mathrm{mm}$
$\delta_{\mathrm{t}} = 10.77\,\frac{\mathrm{kNm}}{\mathrm{m}^3}$

At the nominal condition the motor produces an average torque value $T_{\mathrm{avg}} = 190\,\mathrm{Nm}$ characterized by a torque ripple value $\Delta_T = 9.07\%$. Furthermore, the fundamental airgap flux density peak value is $\hat{B}_{\mathrm{g}} = 1.01\,\mathrm{T}$, having supposed it as starting design assumption equal to $\hat{B}_{\mathrm{g}} = 1\,\mathrm{T}$. Considering a whole electrical period, that is 180 mechanical degrees, the electromagnetic torque profile and airgap flux density harmonic content are showed in fig.[5.6].

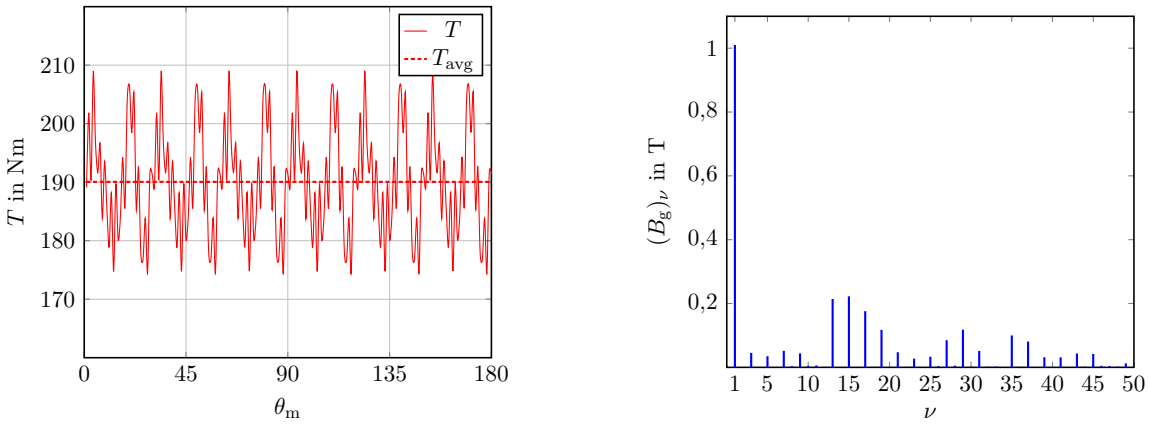

Figure 5.6 – Electromagnetic torque profile and airgap flux density harmonic content

According to the electromagnetic torque harmonic content shown in fig.[5.7], it is possible to individuate the most significant high order harmonics and to improve even more the motor performances deleting them [3]. In particular the 12^{th} electromagnetic torque harmonic presents the highest amplitude value equal to 9.6 Nm.

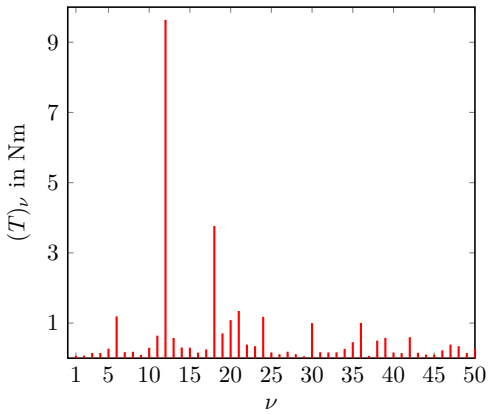

Figure 5.7 – Electromagnetic torque harmonic content

6 The "Machaon" Rotor

Many different strategies have been developed to reduce as much as possible the torque ripple in synchronous reluctance machines. Since the rotor skewing generally adopted in synchronous permanent magnets machines is not enough in synchronous reluctance machines, a smooth torque profile is achieved selecting a proper number of flux barrier per pole N_b and end flux barrier angles per pole θ_b equally distributed along the rotor circumference, as shown in section [3.4.2]. In order to obtain a torque harmonics compensation, the end flux barrier angles per pole θ_b are shifted from their equally spaced position, as represented in section [5.3].

An innovative strategy is to adopt different flux barriers per pole pair geometries in a single rotor lamination [8] [7]. This rotor configuration is called "Machaon" configuration because the different flux barriers geometries remind the homonymous animal drawing wings (see fig.[6.1]).

Considering a two pole pairs $p = 2$ machine, the two different flux barriers geometries are called Romeo "R" and Juliet "J" since they are inseparable. The equal shape poles are symmetrical to the shaft axis avoiding unbalanced rotor. A smoother torque profile is achieved compensating the torque harmonics caused by R-flux barriers geometry adopting a proper geometry for the J-flux barriers.

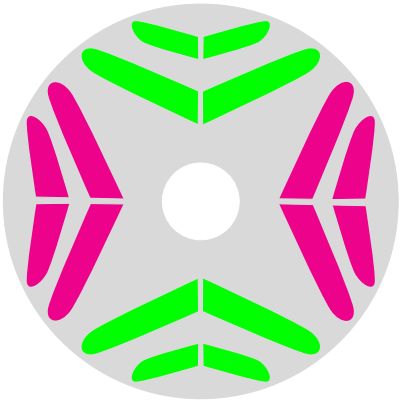

Figure 6.1 – The Machaon rotor configuration

Regarding the current synchronous reluctance motor design, the R-flux barriers geometry has been already defined in chapter [5]. On the contrary the J-flux barriers geometry is defined in order to compensate R-flux barriers torque harmonics.

6.1 J-flux barriers geometry

A suggested method is presented to estimate the J-flux barriers end angles θ_{j} to compensate R-flux barriers torque harmonic [3]. As already said, this method is limited to only one or two flux barriers per pole and then for a more complex rotor geometry this approach can not be applied. Therefore, the J-flux barriers thickness related to J-rotor insulation coefficient $K^{\mathrm{r}}_{\mathrm{air,j}}$ and the J-flux barriers end angles θ_{j} are investigated as already seen for the R-flux barriers in chapter [5].

Keeping fixed the R-rotor insulation coefficient $K^{\mathrm{r}}_{\mathrm{air,r}} = K^{\mathrm{r}}_{\mathrm{air}}$ and the R-flux barriers end angles $\theta_{\mathrm{r}} = \theta_{\mathrm{b}}$, the torque ripple value Δ_T is investigated for the following parameters combinations:

- $0.35 \leq K^{\mathrm{r}}_{\mathrm{air,j}} \leq 0.5$
- $11° \leq \theta_{\mathrm{j},1} \leq 15°$
- $26° \leq \theta_{\mathrm{j},2} \leq 27°$
- $38.75° \leq \theta_{\mathrm{j},3} \leq 40°$

The influence of J-flux barriers thickness variations on the motor electromagnetic torque is shown in fig.[6.2].

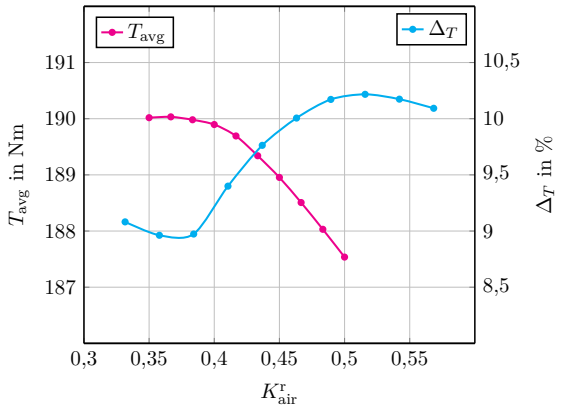

Figure 6.2 – J-rotor insulation coefficient $K^{\mathrm{r}}_{\mathrm{air,j}}$ influence on torque profile

A restrained increase of the J-rotor insulation coefficient $K^{\mathrm{r}}_{\mathrm{air,j}}$ leads to a torque ripple value Δ_T decrease not affecting the average torque value T_{avg}. The J-flux barriers angles $[\theta_{\mathrm{j},1}; \theta_{\mathrm{j},2}; \theta_{\mathrm{j},3}] = [12.75°; 26.5°; 39°]$ combination ensures the lowest torque ripple value approximately equal to $\Delta_T = 8.5\%$ according to fig.[6.3].

Machaon rotor configuration strategy can be improved using optimizing algorithms that consider separately the two different flux barrier geometries from the first rotor design step in order to achieve better results in electromagnetic performances terms.

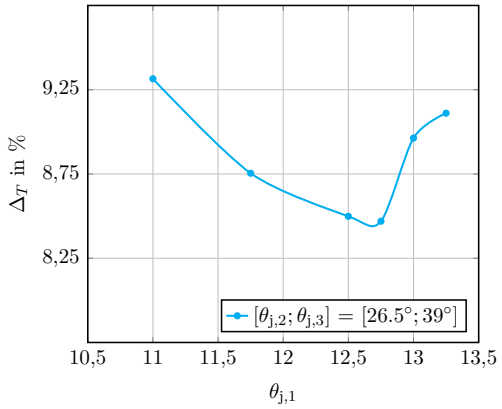

Figure 6.3 – Torque ripple value Δ_T in function of the J-flux barriers angle $\theta_{j,1}$ for a fixed $\theta_{j,2}$ and $\theta_{j,3}$ combination

6.2 Rotor configurations comparison

The single flux barriers geometry and the Machaon rotor configurations are quite similar from a mechanical point of view (see fig.[6.4]).

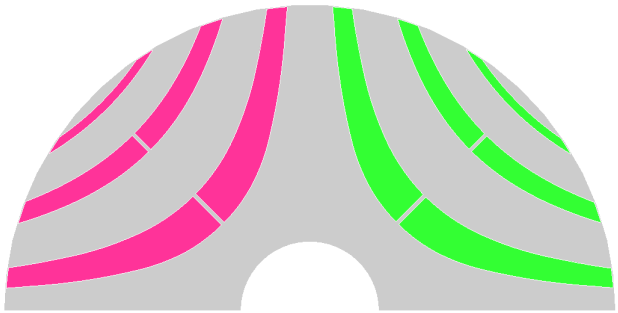

Figure 6.4 – Machaon rotor cross section

The increase of the J-flux barriers angle $\theta_{j,1}$ and of the J-rotor insulation coefficient $K^{\mathrm{r}}_{\mathrm{air,j}}$ causes a consequent radial iron rib increment of the second J-flux barrier $t^{\mathrm{r}}_{\mathrm{rib}}$ in order to guarantee a self-sustained mechanically rotor (see tab.[6.1]). Regarding the end flux barriers shape, considerations explained in section [3.4.6] are adopted for single flux barriers geometry and both Machaon rotor configuration.

Table 6.1 – Machaon geometrical variations

$\theta_{\mathrm{j},1} = 12.75°$
$K^{\mathrm{r}}_{\mathrm{air,j}} = 0.37$
$t^{\mathrm{r}}_{\mathrm{rib},2} = 1.3\,\mathrm{mm}$

Considering a whole electrical period, that is 180 mechanical degrees, the electromagnetic torque profile and airgap flux density harmonic content are showed in fig.[6.5].

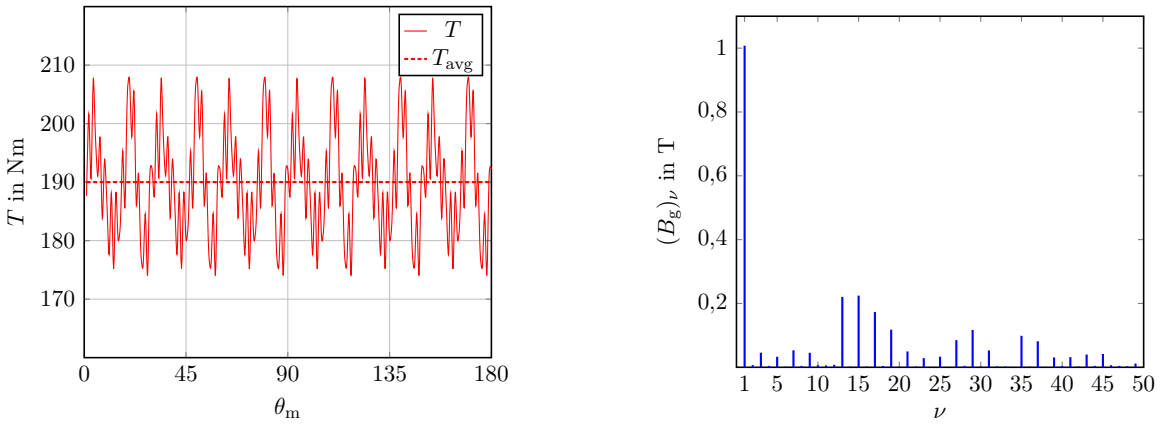

Figure 6.5 – Machaon motor electromagnetic torque profile and airgap flux density harmonic content

From an electromagnetic point of view, the Machaon rotor configuration leads to a torque ripple value Δ_T decrease compared to the single flux barriers geometry configuration. In particular the torque ripple Δ_T relative variation is quantifiable in about -6.3%.

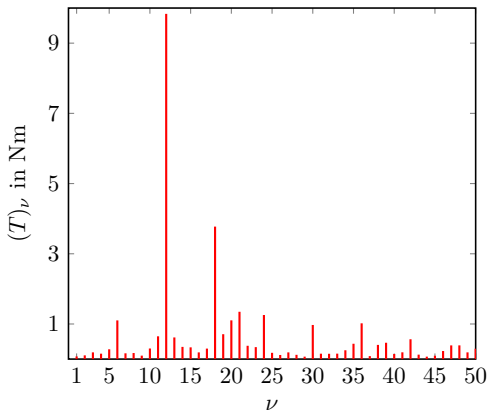

Figure 6.6 – Machaon electromagnetic torque harmonic content

Machaon electromagnetic torque harmonic content is shown in fig.[5.7]. Not only torque harmonics amplitude but also their phase defines the torque ripple value Δ_T. Same order torque harmonics in phase opposition compensate each other involving to a smoother torque profile. As already explained in chapter [6], it is possible to individuate the most significant high order harmonics and to improve even more the motor performances compensating them thanks to different flux barriers geometries [8] [7] [3].

7 Motor Performances Analysis

Concluded the study aims consisting of the design concept derivation and application on specific requirements, a briefly motor performances analysis is considered.

In order to further investigate the design results, some design assumptions are validated. In particular the motor saliency ratio ξ, power factor $\cos(\varphi)$ and efficiency η are calculated and compared to the related design assumptions.

Table 7.1 – Design assumptions validation: saliency ratio ξ, power factor $\cos(\varphi)$ and efficiency η

ξ	$= 10$
$\cos(\varphi)$	$= 0.80$
η	$= 0.95$

7.1 Electromagnetic analysis: saliency ratio ξ

The synchronous reluctance machine figure of merit is the saliency ratio ξ as already explained in section [3.1]. The electromagnetic performances of the machine are related to the saliency ratio ξ and therefore its value can evaluate the validity of a design. In order to avoid the cross-coupling effect and to estimate properly the saliency ratio ξ, the motor is fed separately along the d-axis and q-axis. The linkage fluxes along the d-axis Λ_d and q-axis Λ_q are showed in fig.[7.1].

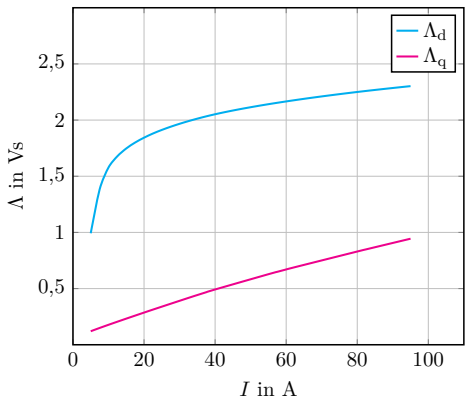

Figure 7.1 – Λ_d and Λ_q linkage fluxes

The d-axis linkage flux Λ_d is affected by the saturation effect as the current I increases. On the contrary the q-axis linkage flux Λ_q is proportional to the current I because it links in large part air magnetic paths.

For the nominal current I_n and the nominal displacement current electrical angle $\alpha_\mathrm{i}^\mathrm{e}$, the saliency ratio ξ is calculated according to its definition:

$$\xi = \frac{L_\mathrm{d}}{L_\mathrm{q}} = \frac{\Lambda_\mathrm{d}}{\Lambda_\mathrm{q}} \cdot \tan(\alpha_\mathrm{i}^e) = 9.35 \tag{7.1}$$

From the saliency ratio ξ, it is possible to estimate the maximum power factor $\cos(\varphi)$:

$$\cos(\varphi) = \frac{\xi - 1}{1 + \xi} = 0.80 \tag{7.2}$$

The saliency ratio ξ and power factor $\cos(\varphi)$ estimation are in line with the design assumption.

7.2 Losses and efficiency η

At the nominal operating condition a fast estimation of the motor losses and efficiency is calculated analytically [6].

Joule losses P_J

In synchronous reluctance machines the Joule losses P_J are localized only in the stator winding. This feature involves benefits in operating temperature and efficiency terms. In order to calculate the electric resistance of a phase R_s, the conductors length L_c and their cross section area in the slot S_c are estimated:

$$L_\mathrm{c} = L_\mathrm{stk} + L_\mathrm{end} = L_\mathrm{c} + 2.5\,\frac{D_\mathrm{s,i}}{p} = 494\,\mathrm{mm} \tag{7.3}$$

$$S_\mathrm{c} = K_\mathrm{fill}\,S_\mathrm{slot} = 54\,\mathrm{mm}^2 \tag{7.4}$$

where L_end is the end winding length.

Assuming an operating temperature of 120° C, the phase electric resistance is obtained:

$$R_\mathrm{s} = \rho_\mathrm{Cu}\,\frac{N_\mathrm{s}\,L_\mathrm{c}}{S_\mathrm{c}} = 0.033\,\Omega \tag{7.5}$$

where ρ_Cu is the copper resistivity at the operating temperature. Finally the Joule losses P_J estimation is:

$$P_\mathrm{J} = 3\,R_\mathrm{s}\,I_\mathrm{n}^2 = 110\,\mathrm{W} \tag{7.6}$$

Iron losses P_{iron}

In synchronous reluctance machines the iron losses P_{iron} in the rotor can be neglected due to the minor impact on the total losses [17]. The magnetic and mechanical features of the stator lamination material are presented in tab.[7.2]. The flux density peak value in the stator teeth and backiron is $\hat{B}_{\text{s}} = 1.7\,\text{T}$ at the nominal frequency $f_{\text{n}} = 50\,\text{Hz}$. According to the material data sheet, the specific total loss is $\delta_{\text{loss}} = 8.58\,\frac{\text{W}}{\text{kg}}$. The stator lamination has suffered manufacturing process that have deteriorated its magnetic properties. In order to take in to account this magnetic worsening, an increasing manufacturing factor $k_{\text{m}} = 1.5$ is considered to evaluate the iron losses P_{iron}:

$$P_{\text{iron}} = k_{\text{m}}\,\delta_{\text{loss}}\,M_{\text{s}} = 890\,W \tag{7.7}$$

where $M_{\text{s}} = 70\,\text{kg}$ is the stator mass.

Table 7.2 – FLU M800 65A data sheet

Specific total loss	$= 3.2\,\frac{\text{W}}{\text{kg}}$ at 1 T and 50 Hz
Mass density	$= 7700\,\frac{\text{kg}}{\text{m}^3}$
Thickness	$= 0{,}35\,\text{mm}$

Mechanical losses P_{m}

The mechanical losses P_{m} are related for example to mechanical frictions, bearings losses, air viscosity and ventilation losses. These losses are not easy to evaluate in advance but they can be estimated according to the following empirical equation:

$$P_{\text{m}} = 0.4\,P_{\text{n}}\,\sqrt{n_{\text{n}}} = 460\,\text{W} \tag{7.8}$$

where P_{n} is the mechanical power of the machine that corresponds to the motor nominal power; and n_{n} is the rotational speed of the rotor.

Stray losses P_{stray}

Stray losses P_{stray} are the additional losses that occur in the machine operation in addition to Joule, iron and mechanical losses. Additional losses are mainly due to leakage fluxes in structural conducting parts of the machine. These leakage fluxes can lead to eddy currents and iron losses. In the design process stray losses P_{stray} are assumed a percentage of the Joule and iron losses due to their difficult analytical estimation.

$$P_{\text{stray}} = 0.10\,(P_{\text{J}} + P_{\text{iron}}) = 100\,\text{W} \tag{7.9}$$

Efficiency η

At last the motor efficiency η can be estimated:

$$\eta = \frac{P_\mathrm{n}}{P_\mathrm{n} + P_\mathrm{J} + P_\mathrm{iron} + P_\mathrm{m} + P_\mathrm{stray}} = 0.95 \tag{7.10}$$

The motor efficiency η estimation is in line with the design assumption. Consequently the nominal active electrical power P_e necessary to supply the motor is:

$$P_\mathrm{e} = \frac{P_\mathrm{n}}{\eta} = 31.415\,\mathrm{kW} \tag{7.11}$$

8 Dual Three-Phase Supply System

As already explained in section [1.1], in order to fully embrace electric mobility as soon as possible, the problems related to this technology must be faced up and solved. The operating conditions of road transport applications are very demanding because they require frequent accelerations and regenerative braking that stress electromagnetically and mechanically the motor. Therefore the powertrain reliability is a key parameter to consider in designing electric motors.

A dual three-phase supply can be adopted to improve the system redundancy and consequently its fault tolerance. This solutions leads also to advantages in energy saving terms. The vehicle range expectancy can be increased supplying partially the motor in proper operation conditions saving energy from the batteries.

In this preliminary study two different configurations of dual three-phase supply in synchronous reluctance motors are investigated. In particular, the electromagnetic torque profile is analytically evaluated in partial operating conditions for a simple synchronous reluctance motor geometry.

8.1 Dual three-phase supply configurations

Consider a three phase two pole pairs synchronous reluctance machine ($2p = 4$) and a one slot per pole and per phase winding ($q = 1$). The machine is supplied by two different inverters Inv_1 and Inv_2 as shown in fig.(8.1). Each inverter feeds the machine with a symmetric and balanced three-phase winding, $\mathrm{A}_1, \mathrm{B}_1, \mathrm{C}_1$ and $\mathrm{A}_2, \mathrm{B}_2, \mathrm{C}_2$, respectively. Two different supplying configurations are feasible and therefore they are investigated in the following.

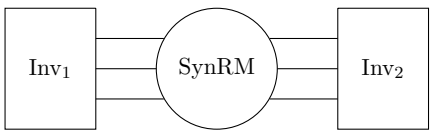

Figure 8.1 – Dual three-phase supply system

The first configuration consists of supplying two consecutive poles by the first inverter Inv_1 and the other pole pair by the second one Inv_2, as shown in fig.(8.2). For this reason, this configuration can be expressed symbolically as (1122). The inverters are sized for the same nominal power $P_{\mathrm{Inv}_1} = P_{\mathrm{Inv}_2}$. The nominal power of the machine is P_{n} and during its healthy operation, the two inverters work. Therefore the power of each inverter is equal to the machine nominal power $P_{\mathrm{Inv}_1} = P_{\mathrm{Inv}_2} = P_{\mathrm{n}}$. Consider a slotless stator and a infinitesimal thickness conductive sheet placed on the inner surface of the stator replacing the conductors within the

slots. A conductors density $n_{\mathrm{d}}(\theta_{\mathrm{s}})$, equivalent to the actual distribution of the coils within the slots, is distributed along the inner stator circumference.

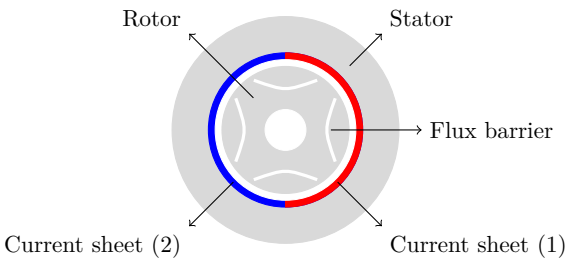

Figure 8.2 – The (1122) pole pairs arrangement

A linear current density distribution along the conductive sheet, called electric loading K_{s}, is considered supplying the actual dual three-phase windings. In the stator reference frame, the fundamental distribution of the electric loading is a linear superposition of the electric loading produced by the first winding $K_{\mathrm{s}}^{(1)}$ and of the electric loading produced by the second winding $K_{\mathrm{s}}^{(2)}$ as shown in fig.(8.3):

$$K_{\mathrm{s}}(\theta_{\mathrm{s}}) = K_{\mathrm{s}}^{(1)}(\theta_{\mathrm{s}}) + K_{\mathrm{s}}^{(2)}(\theta_{\mathrm{s}}) \tag{8.1}$$

The electric loading peak value at $\hat{K}_{\mathrm{s}}$ healthy conditions is equal to the electric loading peak value at partial supply conditions $\hat{K}_{\mathrm{s}} = \hat{K}_{\mathrm{s}}^{(1)} = \hat{K}_{\mathrm{s}}^{(2)}$ since the two inverters are sized for the nominal power $P_{\mathrm{Inv_1}} = P_{\mathrm{Inv_2}} = P_{\mathrm{n}}$ as already said.

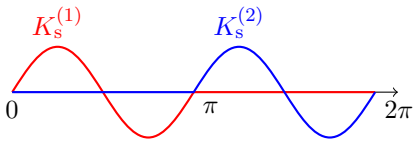

Figure 8.3 – Electric loading distribution in configuration (1122)

Consider the case of inverter $\mathrm{Inv_2}$ is switched off due to a fault or to reduce the motor supply power saving energy, for example, from the batteries of an electric vehicle. Therefore, according to equation (8.1) the fundamental distribution of the electric loading is:

$$K_{\mathrm{s}}(\theta_{\mathrm{s}}) = K_{\mathrm{s}}^{(1)}(\theta_{\mathrm{s}}) \tag{8.2}$$

This windings spatial arrangement leads to a low mutual inductance L_{M} between the two windings $\mathrm{A_1}, \mathrm{B_1}, \mathrm{C_1}$ and $\mathrm{A_2}, \mathrm{B_2}, \mathrm{C_2}$ supplied by the first and second inverter, respectively. Therefore a possible short circuit in the second winding is not supplied by the first winding. In this partial and unbalanced supply of the machine, strong radial forces F_{r} rise on the rotor compromising the regular machine operation and stressing the bearings. At last, the electromagnetic torque $T_{\mathrm{n}}^{(1)}$ produced is intuitively lower than the nominal torque T_{n} generated at healthy operating conditions.

The second configuration consists of supplying alternately each pole by a different inverter, as shown in fig.(8.4). For this reason, this configuration can be expressed symbolically as (1212). Also in this case the inverters are sized for the same nominal power $P_{\mathrm{Inv_1}} = P_{\mathrm{Inv_2}}$. Supplying

properly the windings A_1, B_1, C_1 and A_2, B_2, C_2 in terms of temporal displacement, it is possible to minimize the nominal power of each inverter to $P_{\text{Inv}_1} + P_{\text{Inv}_2} = P_\text{n}$. In the stator reference frame, the fundamental distribution of the electric loading K_s is again expressed as a linear superposition of $K_\text{s}^{(1)}$ and $K_\text{s}^{(2)}$ according to equation (8.1). Assuming α_s the slot pitch angle, the electric loading $K_\text{s}^{(1)}$ and $K_\text{s}^{(2)}$ have a α_s spatial angular displacement. Shifting of α_s the electric loading $K_\text{s}^{(2)}$ in temporal terms, it is possible to add arithmetically the sinusoidal electric loading amplitudes to obtain the total electric loading peak value, $\hat{K}_\text{s}$, as shown in fig.(8.5). Therefore, the electric loading peak value at healthy conditions is equal to $\hat{K}_\text{s} = \hat{K}_\text{s}^{(1)} + \hat{K}_\text{s}^{(2)}$ since the two inverters are sized for half nominal power $P_\text{n} = P_{\text{Inv}_1} + P_{\text{Inv}_2}$ as already said.

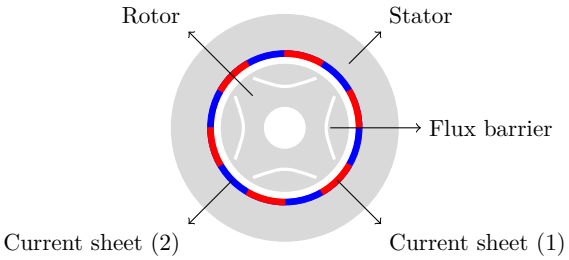

Figure 8.4 – The (1212) pole pairs arrangement

Considering the case of inverter Inv_2 is switched off, the distribution of the fundamental electric loading is expressed according to equation (8.2). Differently form the case of configuration (1122), this windings spatial arrangement leads to a high mutual inductance L_M between the two windings A_1, B_1, C_1 and A_2, B_2, C_2. In the partial supply operation of the machine, do not rise on the rotor strong radial forces F_r and the mechanical stresses are equally distributed along the rotor circumference. Furthermore, the electromagnetic torque $T_\text{n}^{(1)}$ produced is intuitively lower than the nominal torque T_n generated at healthy operating conditions.

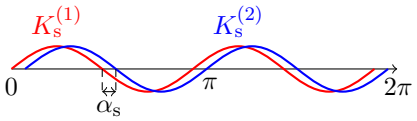

Figure 8.5 – Electric loading distribution in configuration (1212)

8.2 Analytical model for average electromagnetic torque estimation in configuration (1122)

Consider the partial operation of the machine. The distribution of the fundamental electric loading in the stator reference frame is expressed according to equation (8.2). Taking into account the whole machine topology, the electric loading $K_{\text{s},\nu}^{(1)}$ Fourier series expansion is:

$$K_{\text{s},\nu}^{(1)}(\theta_\text{s}) = K_{\text{s},2}(\theta_\text{s}) + K_{\text{s},\nu}(\theta_\text{s}) \tag{8.3}$$

where $K_{s,2}(\theta_s)$ is the electric loading main harmonic:

$$K_{s,2}(\theta_s) = \frac{\hat{K}_s}{2}\sin(2\theta_s - \alpha_i^e) \tag{8.4}$$

and $K_{s,\nu}(\theta_s)$ is the electric loading harmonic content for odd values of the harmonic order, ν:

$$K_{s,\nu}(\theta_s) = \sum_{\nu=1}^{\infty} \frac{4\hat{K}_s}{\pi(4-\nu^2)} \cdot \cos(\nu\theta_s + (\nu-2)\omega t - \alpha_i^e) \tag{8.5}$$

The most significant electric loading harmonics $K_{s,\nu}^{(1)}$ are shown in fig.(8.6).

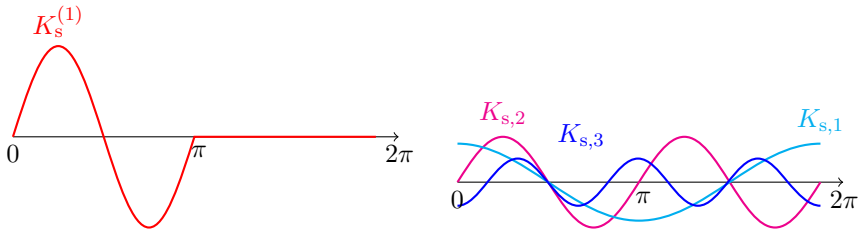

Figure 8.6 – Electric loading $K_s^{(1)}$ Fourier series expansion

In order to estimate the average electromagnetic torque, $T_n^{(1)}$, only the electric loading main harmonic, $K_{s,2}(\theta_s)$, is considered. Since it is synchronous with the rotor, the electric loading main harmonic can be expressed in the rotor system of reference as:

$$K_{s,2}(\theta_r) = \frac{\hat{K}_s}{2}\sin(2\theta_r - \alpha_i^e) \tag{8.6}$$

The stator magnetic potential, that is the stator magneto-motive force distribution along the air-gap is obtained according to Ampere's law:

$$U_{s,2}(\theta_r) = \int \frac{D}{2} K_{s,2}(\theta_r)\,\mathrm{d}\theta_r \tag{8.7}$$

$$= \int \frac{D}{2}\frac{\hat{K}_s}{2}\sin(2\theta_r - \alpha_i^e)\,\mathrm{d}\theta_r \tag{8.8}$$

$$= -\frac{D\hat{K}_s}{8}\cos(2\theta_r - \alpha_i^e) \tag{8.9}$$

Consider a rotor topology with one flux barrier per pole [8]. Assuming q-axis as the minimum permeance axis, the mechanical half-angle θ_b is the flux barrier angle respect to the q-axis and l_b and t_b are the flux barrier length and thickness, respectively. Neglecting the magnetic voltage drop in the stator iron path, the air-gap flux density distribution is:

$$B_g(\theta_r) = \mu_0 \frac{-U_s(\theta_r) + U_r(\theta_r)}{g} \tag{8.10}$$

where U_r is the rotor magnetic potential. The rotor magnetic potential is assumed to be constant in each magnetic island and null elsewhere. Since:

$$\phi_b = \int_{\frac{\pi}{4}-\theta_b}^{\frac{\pi}{4}+\theta_b} -B_g(\theta_r)\frac{DL}{2}\mathrm{d}\theta_r \tag{8.11}$$

$$U_r = \phi_b \cdot R_b \tag{8.12}$$

where ϕ_b and R_b are the magnetic flux that flows through the flux barrier and its magnetic reluctance, respectively. The rotor magnetic potential, $U_{\mathrm{r},2}$, is therefore:

$$U_{\mathrm{r},2} = a \int_{\frac{\pi}{4}-\theta_\mathrm{b}}^{\frac{\pi}{4}+\theta_\mathrm{b}} U_{s,2}(\theta_\mathrm{r})\,\mathrm{d}\theta_\mathrm{r} \tag{8.13}$$

$$= a \int_{\frac{\pi}{4}-\theta_\mathrm{b}}^{\frac{\pi}{4}+\theta_\mathrm{b}} -\frac{D\hat{K}_\mathrm{s}}{8}\cos(2\theta_\mathrm{r} - \alpha_i^\mathrm{e})\,\mathrm{d}\theta_\mathrm{r} \tag{8.14}$$

$$= -\frac{aD\hat{K}_\mathrm{s}}{8}\sin(2\theta_\mathrm{b})\sin(\alpha_i^\mathrm{e}) \tag{8.15}$$

where the dimensionless coefficient a is a function of the rotor geometry, and it is given by:

$$a = \frac{\frac{D}{2g}\frac{t_\mathrm{b}}{l_\mathrm{b}}}{1 + \frac{D}{2g}\frac{t_\mathrm{b}}{l_\mathrm{b}}2\theta_\mathrm{b}} \tag{8.16}$$

The electromagnetic torque is obtained by integrating the Lorentz's force density $B_\mathrm{g}(\theta_\mathrm{r})K_\mathrm{s}(\theta_\mathrm{r})$ along the air–gap surface, and multiplying the result by the radius $\frac{D}{2}$:

$$T_\mathrm{n}^{(1)} = -\frac{D}{2}\int_0^2 \frac{DL}{2}B_\mathrm{g}(\theta_\mathrm{r})K_\mathrm{s}(\theta_\mathrm{r})\,\mathrm{d}\theta_\mathrm{r} \tag{8.17}$$

$$= \frac{\mu_0}{g}\frac{D^2L}{4}\,U_{\mathrm{r},2}\,p \int_{\frac{\pi}{4}-\theta_\mathrm{b}}^{\frac{\pi}{4}+\theta_\mathrm{b}} -2\cdot K_{\mathrm{s},2}(\theta_\mathrm{r})\,\mathrm{d}\theta_\mathrm{r} \tag{8.18}$$

$$= \frac{1}{4}\frac{\mu_0}{g}\left(\frac{D}{2}\right)^3 L\,\hat{K}_\mathrm{s}^2\sin(2\alpha_i^\mathrm{e})\,a\sin^2(2\theta_\mathrm{b}) \tag{8.19}$$

Assuming T_n the electromagnetic torque in healthy operating conditions:

$$T_\mathrm{n} = \frac{\mu_0}{g}\left(\frac{D}{2}\right)^3 L\,\hat{K}_\mathrm{s}^2\sin(2\alpha_i^\mathrm{e})\,a\sin^2(2\theta_\mathrm{b}) \tag{8.20}$$

the ratio between the electromagnetic torque generated in partial and in healthy operating conditions is:

$$\frac{T_\mathrm{n}^{(1)}}{T_\mathrm{n}} = \frac{1}{4} \tag{8.21}$$

This result finds an intuitive physical validation because a half machine is supplied by a half of the main electric loading harmonic and consequently the average electromagnetic torque generated at the shaft is a quarter of the nominal one in healthy conditions.

8.2.1 Analytical model for electromagnetic torque ripple estimation in configuration (1122)

Consider now only the electric loading harmonic content $K_{\mathrm{s},\nu}(\theta_\mathrm{s})$. In the rotor system of reference, the electric loading harmonic content, $K_{\mathrm{s},\nu}$, consists of a sub-harmonic for $\nu = 1$ and odd high order harmonics for $\nu \geq 3$:

$$K_{\mathrm{s},\nu}(\theta_\mathrm{r}) = K_{\mathrm{s},1}(\theta_\mathrm{r}) + K'_{\mathrm{s},\nu}(\theta_\mathrm{r}) \tag{8.22}$$

where $K_{\mathrm{s},1}(\theta_\mathrm{r})$ is the electric loading sub-harmonic:

$$K_{\mathrm{s},1}(\theta_\mathrm{r}) = \frac{4\,\hat{K}_\mathrm{s}}{3\pi} \cdot \cos(\theta_\mathrm{r} - \omega t - \alpha_i^\mathrm{e}) \tag{8.23}$$

and $K'_{\mathrm{s},\nu}(\theta_\mathrm{r})$ is the electric loading high order harmonic content for $\nu \geq 3$ and odd:

$$K'_{\mathrm{s},\nu}(\theta_\mathrm{r}) = \sum_{\nu=3}^{\infty} \frac{4\,\hat{K}_{\mathrm{s},1}}{\pi(4-\nu^2)} \cdot \cos(\nu\theta_\mathrm{r} + (\nu-2) - \alpha_i^\mathrm{e}) \tag{8.24}$$

The resulting sub-harmonic stator magnetic potential, $U_{\mathrm{s},1}(\theta_\mathrm{r})$, is:

$$U_{\mathrm{s},1}(\theta_\mathrm{r}) = \frac{2\,D\,\hat{K}_\mathrm{s}}{3\pi} \cdot \sin(\theta_\mathrm{r} - \omega t - \alpha_i^\mathrm{e}) \tag{8.25}$$

According to equation (8.17), the electromagnetic torque oscillation due to the electrical loading sub-harmonic is null since $K_{\mathrm{s},1}(\theta_\mathrm{r})$ and $U_{\mathrm{s},1}(\theta_\mathrm{r})$ are orthogonal functions. Then, only the electric loading high order harmonic content, $K'_{\mathrm{s},\nu}(\theta_\mathrm{r})$, will be considered in order to evaluate the electromagnetic torque ripple. The resulting high order harmonic content stator magnetic potential, $U'_{\mathrm{s},\nu}$, is:

$$U'_{\mathrm{s},\nu}(\theta_\mathrm{r}) = \frac{2\,D}{\pi} \sum_{\nu=3}^{\infty} \frac{\hat{K}_\mathrm{s}}{\nu(4-\nu^2)} \cdot \sin(\nu\theta_\mathrm{r} + (\nu-2) - \alpha_i^\mathrm{e}) \tag{8.26}$$

As already seen for the main electromagnetic torque harmonic, the rotor magnetic potential high order harmonic content, $U'_{\mathrm{r},\nu}$, can be expressed as following:

$$U'_{\mathrm{r},\nu} = \frac{4}{\pi} a\,D \sum_{\nu=1}^{\infty} \frac{\hat{K}_\mathrm{s}}{\nu^2(4-\nu^2)} \cdot \sin(\nu\theta_\mathrm{b}) \sin(\lambda_\nu) \tag{8.27}$$

where $\lambda_\nu = \frac{\nu k}{4} + (\nu-2)\omega t - \alpha_i^\mathrm{e}$. Finally, the electromagnetic torque high order harmonic content is:

$$T_\nu = -\frac{\mu_0}{g}\frac{16}{\pi^2} D^3 L \sum_{\nu=3}^{\infty} \frac{\hat{K}_\mathrm{s}^2}{\nu^3(4-\nu^2)} a \sin^2(\nu\theta_\mathrm{b})\, \sin(2\lambda_\nu) \tag{8.28}$$

Accordingly, the ν-electromagnetic torque harmonic, τ_ν, can be expressed as:

$$\tau_\nu = \left[-\frac{\mu_0}{g}\frac{16}{\pi^2} D^3 L \frac{\hat{K}_{\mathrm{s},1}^2}{\nu^3(4-\nu^2)} a \sin^2(\nu\theta_\mathrm{b})\right] \sin(2\lambda_\nu) \tag{8.29}$$

$$= A_\nu \cdot \sin\left((2\nu-4)\omega t + \frac{\nu\pi}{2} - 2\alpha_i^\mathrm{e}\right) \tag{8.30}$$

where A_ν is the ν-electromagnetic torque harmonic amplitude. For $\alpha_i^\mathrm{e} = \frac{\pi}{4}$, the ν-electromagnetic torque harmonic results:

$$\tau_\nu = A_\nu \cdot \sin\left((2\nu-4)\omega t + (\nu-1)\frac{\pi}{2}\right) \tag{8.31}$$

It is notable to investigate the relative ν-electromagnetic torque harmonic amplitude respect to the average electromagnetic torque $T_\mathrm{n}^{(1)}$:

$$a_\nu = \frac{\mathrm{A}_\nu}{T_\mathrm{n}^{(1)}} = -\frac{8^3}{\pi^2\nu^3(4-\nu^2)} \frac{\sin^2(\nu\theta_\mathrm{b})}{\sin^2(2\theta_\mathrm{b})} \tag{8.32}$$

The relative amplitude of the most significant electromagnetic torque harmonics, a_ν, is presented in tab.(8.1), having assumed the optimal flux barrier electrical angle θ_b for this rotor topology equal to $\frac{3\pi}{4}$:

Table 8.1 – Electromagnetic torque harmonics relative amplitude a_ν

ν	a_ν in %
3	3.84
5	0.04
7	0.0037

8.3 Analytical model for average electromagnetic torque estimation in configuration (1212)

According to sections [8.1] and [8.2], the electric loading main torque harmonic to consider is:

$$K_{\mathrm{s}}^{(1)}(\theta_{\mathrm{s}}) = \hat{K}_{\mathrm{s}}^{(1)} \sin(2\theta_{\mathrm{s}} - \alpha_i^{\mathrm{e}}) \tag{8.33}$$

The electromagnetic torque generated in partial operating conditions is therefore:

$$T_{\mathrm{n}}^{(1)} = \frac{\mu_0}{g} \left(\frac{D}{2}\right)^3 L \left(\hat{K}_{\mathrm{s}}^{(1)}\right)^2 \sin(2\alpha_i^{\mathrm{e}})\, a \sin^2(2\theta_{\mathrm{b}}) \tag{8.34}$$

The ratio between the electromagnetic torque generated in partial and in healthy operating conditions is:

$$\frac{T_{\mathrm{n}}^{(1)}}{T_{\mathrm{n}}} = \left(\frac{\hat{K}_{\mathrm{s}}^{(1)}}{\hat{K}_{\mathrm{s}}}\right)^2 \tag{8.35}$$

The electric loading peak value, $\hat{K}_{\mathrm{s}}$, can be expressed as:

$$\hat{K}_{\mathrm{s}} = \frac{3 k_{\mathrm{w}} N_{\mathrm{s}} \hat{I}_{\mathrm{n}}}{\pi D} \tag{8.36}$$

where k_{w} is the winding coefficient and N_{s} is the number of equivalent series conductors per phase. The ratio obtained in equation (8.35) can be expressed also as:

$$\frac{T_{\mathrm{n}}^{(1)}}{T_{\mathrm{n}}} = \frac{1}{4} \left(\frac{k_{\mathrm{w}}^{(1)}}{k_{\mathrm{w}}}\right)^2 \tag{8.37}$$

since $N_{\mathrm{s}} = N_{\mathrm{s}}^{(1)}$ and $I_{\mathrm{n}} = 2\, I_{\mathrm{n}}^{(1)}$. Furthermore, for $q = 1$, the ratio between the electromagnetic torque generated in partial and in healthy operating conditions is:

$$\frac{T_{\mathrm{n}}^{(1)}}{T_{\mathrm{n}}} = \frac{1}{4} \tag{8.38}$$

Supplying half machine with a half nominal power inverter, the electromagnetic torque value generated at the shaft is a quarter of the nominal one in healthy conditions.

9 Conclusions

The analytical design concept proves to be valid and solid in its entirety. The starting design assumptions are validated in the analysis step and the application requirements are satisfied by the design results. In particular the main performance advantages of synchronous reluctance machines that is high efficiency η and high torque density are maintained. In addition the drawbacks are limited to acceptable values. For example the power factor $\cos(\varphi)$ is maximized obtaining an high saliency ratio ξ, whereas the torque ripple Δ_T must be further improved although it reached standard values.

In chapter [2] an analytical sizing method for synchronous reluctance machines is derived. The sizing method relates the electrical and magnetic loading of the machine to its main dimensions, as showed by equation (2.77). The general validity of this method allows to consider any applications characterized by specific requirements. For example the maximum space available is a boundary condition that could be taken into account from the first sizing step without losing any validity. Furthermore, the synchronous reluctance machines sizing method is comparable to the synchronous machines one based on Lorentz force law. Therefore, for a fixed electromagnetic loading or for fixed dimensions it is possible to compare different machine typologies investigating the most suitable solution for a specific application.

In chapter [3] the analytical design concept is analyzed. Starting from the magnetic loading assumption, the electrical loading and the machine size are obtained. This is not the only one valid approach. For example, the cooling system effectiveness defines the maximum stator current density achievable and consequently the electrical loading of the machine. Therefore, it is possible to assume the electrical loading in order to maximize the ratio between the electromagnetic torque generated at the shaft and the size of the machine designing in high torque density terms. Successively the stator and rotor geometry are designed. The stator geometry is not examined in detail due to its widely spread in literature. A more refined stator design involves to machine performances improvements, even though a proper winding arrangement is already adopted. For example the stator electrical loading harmonic content and leakage inductances could be further limited investigating more deeply the slots shape. The rotor topology design is considered with particular attention from an electromagnetic and both mechanical point of view. The parameters influencing motor performances are individually investigated in order to identify the trade-offs between the electromagnetic and mechanical performances of the motor. Angular position, thickness and shape of the flux barriers are defined analytically according to a solid and orderly procedure. In order to guarantee a mechanically self-sustained rotor, proper arrangements are adopted considering static and fatigue stress analysis. The rotor geometry drawing procedure could be improved implementing optimizing algorithms. In particular an automatic and dynamics drawing algorithm for flux barriers shape could lead to improvements in torque ripple terms. More precise geometrical solutions could be obtained through a fluid and not discretized topology investigation. For example, the "Machaon" rotor configuration presented in chapter [6], could

be adopted from the first step of design using proper optimizing algorithms in order to find more suitable geometrical solutions thanks to more degrees of freedom.

In chapter [4] the analytical design concept is applied to given motor specifications and successively the machine design is analyzed by the finite elements software Flux2D by Altair in chapters [5] and [7]. The final design presents a nominal torque value T_n of 190 Nm at the rotational speed n_n of 1500 rmp. In chapter [6] the "Machaon" rotor configuration is adopted leading to a torque ripple value Δ_T equal to 8.5%. The relative decrease of the torque ripple value Δ_T is about 6.3% compared to the single flux barriers geometry configuration value. The motor exhibits an efficiency of 95% and a volumetric torque density of 10.5 $\frac{\mathrm{kNm}}{\mathrm{m}^3}$. Furthermore, the design assumptions are validated in the design analysis confirming the design concept validity. For example, the end flux barrier angles assumption proved to be very close to the improved solution obtained by finite elements simulations. Indeed the end flux barrier angles assumption combination was $[\theta_{\mathrm{b},1}; \theta_{\mathrm{b},2}; \theta_{\mathrm{b},3}] = [13°; 26°; 39°]$, whereas regarding the final design it is $[\theta_{\mathrm{r},1}; \theta_{\mathrm{r},2}; \theta_{\mathrm{r},3}] = [13°; 26.5°; 39°]$ for the R-flux barriers geometry and $[\theta_{\mathrm{j},1}; \theta_{\mathrm{j},2}; \theta_{\mathrm{j},3}] = [12.75°; 26.5°; 39°]$ for the J-flux barriers geometry. These contained variations led to a 35% torque ripple value Δ_T relative decrease. At last, the motor reaches a saliency ratio ξ value equal to 9.35 and a maximum power factor achievable $\cos(\varphi)$ value equal to 0.80, which are near to the starting assumptions fixed to 10 and 0.80 respectively.

Concluding, the analytical design concept derivation and application could be adopted as design basis to any applications characterized by specifics requirements ensuring suitable results thanks to its ductility and general validity.

Bibliography

[1] ABB. *Low voltage IE4 synchronus reluctance motors*. August 2016. URL: http://new.abb.com/motors-generators/iec-low-voltage-motors/frequency-controlled-motors/synchronous-reluctance-motor-drive-packages/ie4-synrm-motor-drive-packages.

[2] ABB. *Searching for cost efficient efficiency*. opened on 05.03.2018 at 11:44. URL: http://new.abb.com/drives/media/cost-efficient-efficiency.

[3] Bacco and Bianchi. "Choice of Flux-Barriers Position in Synchronous Reluctance Machines". In: *IEEE Energy Conversion Congress & Expo : Cincinnati, Ohio, October 1-5* (2017). URL: http://ieeexplore.ieee.org/servlet/opac?punumber=8085404.

[4] Barcaro, Meneghetti, and Bianchi. "Structural Analysis of the Interior PM Rotor Considering Both Static and Fatigue Loading". In: *IEEE Transactions on Industry Applications* 50.1 (2014), pp. 253–260. ISSN: 0093-9994. DOI: 10.1109/TIA.2013.2268048.

[5] Bianchi. *Calcolo delle macchine elettriche col metodo degli elementi finiti*. CLEUP, 2001. ISBN: 8871785282.

[6] Bianchi and Bolognani. *Metodologia di progettazione delle macchine elettriche*. CLEUP, 2001. ISBN: 8871785290.

[7] Bianchi et al. "Rotor Flux-Barrier Design for Torque Ripple Reduction in Synchronous Reluctance and PM-Assisted Synchronous Reluctance Motors". In: *IEEE Transactions on Industry Applications* 45.3 (2009), pp. 921–928. ISSN: 0093-9994. DOI: 10.1109/TIA.2009.2018960.

[8] Bianchi et al. "Torque Harmonic Compensation in a Synchronous Reluctance Motor". In: *IEEE Transactions on Energy Conversion* 23.2 (2008), pp. 466–473. ISSN: 0885-8969. DOI: 10.1109/TEC.2007.914357.

[9] Bolognani, Mahmoud, and Bianchi. "Fast synthesis of permanent magnet assisted synchronous reluctance motors". In: *IET Electric Power Applications* 10.5 (2016), pp. 312–318. ISSN: 1751-8660. DOI: 10.1049/iet-epa.2015.0240.

[10] Di Nardo et al. *End Barrier Shape Optimizations and Sensitivity Analysis of Synchronous Reluctance Machines: 41st Annual Conference of the IEEE Industrial Electronics Society : November 9-12, 2015, Pacifico Yokohama, Yokohama, Japan*. Piscataway, NJ. URL: http://ieeexplore.ieee.org/xpl/mostRecentIssue.jsp?punumber=7378180.

[11] European Environment Agency. *Driving to an electric future?* opened on 06.03.2018 at 08:49. URL: https://www.eea.europa.eu/signals/signals-2017/articles/driving-to-an-electric-future.

[12] European Environment Agency. *GHG emissions by aggregated sector*. 24 Nov 2017. URL: https://www.eea.europa.eu/data-and-maps/daviz/ghg-emissions-by-aggregated-sector-1#tab-dashboard-02.

[13] European Environment Agency. *Total greenhouse gas emission trends and projections*. 24 Nov 2017. URL: https://www.eea.europa.eu/data-and-maps/indicators/greenhouse-gas-emission-trends-6/assessment-1.

[14] Ferrari, Bianchi, and Fornasiero. *Rotor Saturation Impact in Synchronous Reluctance and PM Assisted Reluctance Motors*. Piscataway, NJ. URL: http://ieeexplore.ieee.org/servlet/opac?punumber=6624149.

[15] FIA and Formula E. *Introducing: the gen2 Formula E car*. opened on 05.03.2018 at 11:42. URL: http://www.fiaformulae.com/en/news/2018/january/introducing-the-gen2-formula-e-car/.

[16] Gamba, Pellegrino, and Cupertino. *Optimal Number of Rotor Parameters for the Automatic Design of Synchronous Reluctance Machines*. Piscataway, NJ. URL: http://ieeexplore.ieee.org/servlet/opac?punumber=6945619.

[17] Guenther and Hofmann. "Multi-Objective Tradeoffs in the Design Optimization of Synchronous Reluctance Machines for Electric Vehicle Application". In: ().

[18] McLaren Applied Technologies. *E-Motor*. opened on 05.03.2018 at 11:03. URL: https://www.mclaren.com/appliedtechnologies/products/item/e-motor-120kw-130nm/.

[19] Moghaddam. "Synchronous Reluctance Machine (SynRM) Design". PhD thesis. Stockholm: Royal Institute of Technology, 2007.

[20] Petrella. "Principi di conversione elettromeccanica dell'energia". In: 2001 (). URL: www.diegm.uniud.it.

[21] Pyrhönen, Jokinen, and Hrabovcová. *Design of Rotating Electrical Machines: Three-phase squirrel cage motor with a two layer integral slot winding and totally enclosed fan cooling*. John Wiley and Sons, Ltd, 2008. ISBN: 978-0-470-69516-6.

[22] Schillingmann, Heister, and Henke. "Scaling Process of Synchronous Reluctance Machines for Automotive Applications: Chicago, Illinois, June 22-24, 2017". In: (2017). URL: http://ieeexplore.ieee.org/servlet/opac?punumber=7984424.

[23] Taghavi and Pillay. "A Sizing Methodology of the Synchronous Reluctance Motor for Traction Applications". In: *IEEE Journal of Emerging and Selected Topics in Power Electronics* 2.2 (2014), pp. 329–340. ISSN: 2168-6777. DOI: 10.1109/JESTPE.2014.2299235.

[24] Inc. Tesla. *Model 3 Emergency Response Guide*. 2017. URL: https://www.tesla.com/sites/default/files/downloads/2017_Model_3_Emergency_Response_Guide_en.pdf.

[25] Vagati et al. "Design criteria of high performance synchronous reluctance motors". In: (), pp. 66–73. DOI: 10.1109/IAS.1992.244463.

[26] White and Woodson. *Electromechanical energy conversion*. John Wiley & Sons, New York, 1959. ISBN: 9780262230292.

[27] Wu et al. "Unified Equivalent MMF Concept for Torque Analysis of AC Machines: 21-24 May 2017". In: (2017). URL: http://ieeexplore.ieee.org/servlet/opac?punumber=7995554.

List of Figures

List of Tables